Available online at www.sciencedirect.com

ScienceDirect

journal homepage: www.elsevier.com/locate/he

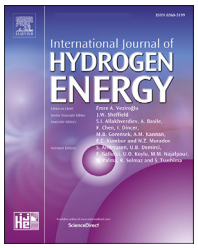

An integrated 0D/1D/3D numerical framework to predict performance, emissions, knock and heat transfer in ICEs fueled with NH_3–H_2 mixtures: The conversion of a marine Diesel engine as case study

Fabio Berni [a,*], *Valentina Pessina* [a], *Luigi Teodosio* [b], *Alessandro d'Adamo* [a], *Massimo Borghi* [a], *Stefano Fontanesi* [a]

[a] *Università degli Studi di Modena e Reggio Emilia, Dipartimento di Ingegneria "Enzo Ferrari", Via Pietro Vivarelli 10, 41125 Modena, Italy*

[b] *Università degli Studi Federico II di Napoli, Dipartimento di Ingegneria Industriale "Federico II", Via Claudio 21, Napoli, Italy*

HIGHLIGHTS

- An integrated 0D/1D/3D numerical framework for CFD simulations is proposed.
- The numerical framework is intended for ICEs fueled with NH_3–H_2 mixtures.
- The framework is tested to convert a marine Diesel engine to NH_3–H_2 mixtures.
- NH_3–H_2 mixtures are effective Diesel substitutes in terms of performance.
- NH_3–H_2 mixtures suffer from NO_x formation even at very lean conditions.

ARTICLE INFO

Article history:
Received 28 May 2023
Received in revised form
28 August 2023
Accepted 15 September 2023
Available online 10 October 2023

Keywords:
e-fuel
Hydrogen
Ammonia
Marine engine
Internal combustion engine
CFD

ABSTRACT

In the maritime transportation, e-fuels represent a valid alternative to fossil energy sources, in order to accomplish the European Union goals in terms of climate neutrality. Among the e-fuels, the ammonia-hydrogen mixtures can play a leading role, as the combination of the two allows to exploit the advantages of each one, simultaneously compensating their gaps.

The main goal of the present publication is the proposal of a robust numerical framework based on 0D, 1D and 3D tools for CFD analyses of internal combustion engines fueled with ammonia-hydrogen mixtures.

The 1D engine model provides boundary conditions for the multi-dimensional investigations and estimates the overall engine performance. 3D in-cylinder detailed analyses are proficiently used to predict combustion efficiency (via the well-established G-equation model supported by laminar flame speed correlations for both ammonia and hydrogen) and emissions (with a detailed chemistry based approach). Heat transfer and knock tendency are evaluated as well, by in-house developed models. As for the 0D/1D chemical kinetics calculations, firstly they support 3D analyses (for example via the generation of ignition delay time tables). Moreover, they allow insights on aspects such as NO_x formation, to individuate mixture qualities able to strongly reduce the emissions.

* *Corresponding author.*
E-mail address: fabio.berni@unimore.it (F. Berni).

https://doi.org/10.1016/j.ijhydene.2023.09.158

The present paper offers also indications for designers on the effectiveness of NH_3–H_2 as valid substitutes of traditional fuels in marine applications. In fact, the proposed framework is preliminary tested to convert an existing marine Diesel engine to ammonia-hydrogen mixtures. Different proportions (among the two fuels) are investigated, included pure ammonia and pure hydrogen and the NH_3–H_2 80mol%-20mol% mixture is selected as the best compromise. Thanks to both the anti-knock quality of the ammonia and the (limited) addition of hydrogen as combustion enhancer, the engine supplied with NH_3–H_2 mixtures is able to operate free of knock and keep the same performance as the original one. Simultaneously (neglecting the presence of lubricant oil in the combustion chamber) unburned hydrocarbons, carbon monoxide and carbon dioxide are eliminated. Still in comparison with the Diesel version, the heat transfer is similar, the NO_x formation is much greater and the engine range (here evaluated in terms of working hours) noticeably reduces.

1. Introduction

The climate neutrality claimed by the European Union (EU) within 2050 [1] will force a huge reduction of greenhouse gas (GHG) emissions (such as carbon dioxide) in the next few years. Since the transportation is one of the main responsibles of CO_2 production [2,3], it will be largely impacted by future legislation. In automotive, EU has already imposed severe limitations with the recent ban to internal combustion engines (ICEs) fueled with traditional fossil fuels starting from 2035. This is pushing car manufacturers towards an intense electrification of their fleets. As for the maritime transportation, european legislation will be less restrictive since alternative solutions such as electrification are less straightforward, mostly for very large cargo ships. In this case, biofuels [4–6] or e-fuels [7–9] seem to be more attractive. In fact, a well-consolidated technology such as the internal combustion engine can be still adopted while keeping an overall carbon-neutrality. For example, considering biodiesel, if the CO_2 absorbed by the crop compensate for the GHG at the exhaust due to combustion, the fuel is carbon-neutral that is the net CO_2 emission null. Taking into account hydrogen, one of the most promising e-fuels, it is carbon-free. Moreover, it can be considered carbon-neutral if produced via electrolysis and the used electricity comes from renewable sources. Besides H_2, another e-fuel that is gaining popularity is ammonia, mostly in combination with the hydrogen itself. Compared to pure H_2 or pure NH_3, mixtures of the two are more appealing as substitutes of traditional fuels (such as Diesel). In fact, despite the very promising combustion-related properties reported in Table 1, hydrogen suffers noticeable problems of storage. Even at liquid phase (which requires cryogenic temperatures, i.e. $\ll 100\,K$, not easy to achieve), its density is nearly one order of magnitude lower than the Diesel one. At gaseous phase, even a compression up to $700\,bar(a)$ would not ensure a storage of hydrogen sufficient for an autonomy comparable to the one provided by Diesel. In addition, such a compression-based technology is expensive and not suitable for long term storage [10].

Other drawbacks related to the use of hydrogen are pre-ignition and backfire. The first is due to hot spots inside the chamber (such as spark-plug or deposits) that easily ignite hydrogen because of the small value of the Minimum Ignition Energy (MIE) compared to traditional fuels such as gasoline, as visible in Table 1. The second takes place in case of port injection as a consequence of a pre-ignition that occurs during the intake stroke. Alternatively, backfire can occur (still in case of port injection) as the flame goes back in the intake port even if valves are closed. This is possible because of the very reduced quenching distance (a comparison with gasoline is visible once again in Table 1).

Conversely, NH_3 at liquid phase (pretty easy to be obtained, since a compression to $10\,bar(a)$ is enough at ambient temperature) has a density similar to traditional fuels. Moreover, it is characterized by a very high anti-knock quality. However, ammonia suffers reduced Lower Heating Value (LHV) and Laminar Flames Speed (LFS). In addition, the energy required for ignition is higher with respect to hydrogen and traditional fuels. In this scenario, NH_3–H_2 mixtures can be proficiently adopted so that the two fuels can mutually compensate their deficiencies. Ammonia and hydrogen properties are resumed in Table 1 and compared with gasoline and Diesel ones.

Compared to traditional fuels, the advantage of NH_3–H_2 mixtures relies in the elimination not only of the principal GHG (namely CO_2), but also of many tailpipe emissions. UHC, CO and soot (particulate matter) disappear, as carbon is not present anymore in the fuel composition. NO_x are the only pollutants remaining at the exhaust. To be fair, it is important to point out that a complete elimination of the previously indicated pollutants (such as UHC) cannot be completely satisfied, because of the production due to the traces of lubricating oil on the combustion chamber walls that inevitably take part to the reactions.

The adoption of ammonia-hydrogen mixtures is not a novelty in the engine panorama. Review articles as well as numerical and experimental studies are available in literature.

Table 1 – Comparison in terms of properties between ammonia, hydrogen, gasoline and Diesel [10–34]. For such fuels (especially for the latter), the proposed values are only indicative, as properties are strongly related to both quality and provenience of the fuel.

Properties	NH_3	H_2	Gasoline	Diesel
Storage	Liquid	Compressed	Liquid	Liquid
Storage temperature [K]	300	300	300	300
Storage pressure [MPa]	1.1	70	0.1	0.1
Density under storage conditions [kg/m^3]	600	39	740	840
Density (standard conditions) [kg/m^3]	0.703	0.082	740	840
Lower Heating Value (LHV) [MJ/kg]	18.8	121	43.5	42.7
Volumetric energy density (storage conditions) [$GJ/\ m^3$]	11.3	4.7	33	35.7
Stoichiometric air-fuel ratio (by mass)	6.05	34.29	14.5	14.5
LFS @ $\varphi = 1$ (standard conditions) [m/s]	0.07	2	0.4	0.8
Auto-ignition Temperature [K]	930	858	550	503
Research Octane Number (RON)	130	>100	98	15
Flammability limits in air (standard conditions) [vol%]	15–28	4.7–75	0.6–8	0.6–5.5
Flammability limits in air (standard conditions) in terms of Φ	0.6–1.4	0.1–7.1	0.3–4.1	0.5–5
Minimum Ignition Energy @ $\varphi = 1$ (standard conditions) [mJ]	8	0.018	0.2	0.63
Quenching Distance @ $\varphi = 1$ (standard conditions) [mm]	7	0.64	2	–

The current status of the development of engines fueled with ammonia-hydrogen blends has been extensively reviewed in Refs. [28,35–37].

Moving to the experimental investigations, tests were proficiently employed to develop/improve chemical kinetics mechanisms [38] or evaluate ignition delay times [39] and laminar flame speed [40,41] of ammonia-hydrogen mixtures. Moreover, several works [19–22,27,42–53] deal with experimental activities aiming at evaluating the potential of ammonia and hydrogen to replace traditional fuel without penalizing engine performance and NO_x formation. HCCI combustion of ammonia-hydrogen mixtures is also investigated [10,54]. In Refs. [55,56], an on-board generation system of H_2 from NH_3 was developed and tested for the production of ammonia-hydrogen mixtures to be adopted in an ICE. In Ref. [57], NH_3– H_2 mixtures were exploited to fuel an engine utilized as a range extender in a hybrid vehicle.

As for the numerical studies, even in this case fundamental aspects such as chemical kinetics mechanism reliability, ignition delay times, laminar and turbulent flame speeds as well as emissions formation were investigated [58–67]. Moreover, numerical analysis dealing with the virtual conversion of existing engines to ammonia-hydrogen mixtures and aiming at evaluating performance and emissions are proposed in Refs. [26,68–76]. In these papers, besides a more traditional solution based on spark plug, HCCI and Diesel injection ignition are also tested.

From the literature review, it is evident the lack of a comprehensive numerical framework able to investigate all the main aspects involved in the application of ammonia-hydrogen mixtures to ICEs and also to simulate traditional fuels (such gasoline or Diesel) for comparison. As a consequence, there is no numerical study where an all-encompassing set of results able to provide a feedback on the potential of ammonia-hydrogen mixtures to replace traditional fuels is presented.

The main goal of the present publication is the proposal of a robust and comprehensive framework to investigate internal combustion engines powered by NH_3–H_2 mixtures. Also traditional fuels, such as gasoline or Diesel, can be simulated by the proposed CFD methodology, for comparison with NH_3–H_2 mixtures thus highlighting pros and cons of the latter. The numerical framework relies on 0D, 1D and 3D tools and aims at predicting engine performance, combustion efficiency, NO_x emissions, heat transfer and knock, thanks to well-established or in-house developed models.

In order to test the framework and provide designers with general indications on the capabilities of NH_3–H_2 mixtures to replace traditional fuels, the second goal is the proposal of an exhaustive set of results by a virtual conversion of an existing marine Diesel engine to ammonia-hydrogen mixtures. For simplicity, just a single cylinder is accounted for, whose operation with Diesel fuel was experimentally investigated in the past [77]. The single cylinder prototype was purposely manufactured to allow experiments in a bench designed to test light duty engines, characterized by total displacements much smaller than the one of the starting marine Diesel engine. Different NH_3–H_2 mixtures are tested, included extreme cases, i.e. only NH_3 or only H_2. The role of CFD is to evaluate the actual capabilities of NH_3–H_2 mixtures to substitute traditional fuels, by comparison with the original version of the powertrain. In particular, the 1D model of the engine estimates the performance moving to the NH_3–H_2 mixtures, besides providing boundary conditions for the 3D in-cylinder simulations. The latter predict combustion efficiency, NO_x emissions, heat transfer and knock tendency. 0D/1D chemical kinetics simulations support 3D analyses (with tables of autoignition delay times) and allow insights on aspects such as LFS and NO_x formation, in order to investigate the possibility to reduce nitrogen oxides for particular ranges of mixture quality.

Compared to the existing literature, the present paper proposes a different and more robust numerical setup, especially for the in-cylinder 3D simulations of ammonia and hydrogen. In other words, the ensemble of the models has never been used before for the investigation of NH_3–H_2 mixtures and it should increase the predictive capabilities of the CFD. Moreover, the overall framework based on the integration of 0D, 1D and 3D tools is another distinctive element of this work that cannot be found in literature, as it allows the

investigation of all the main aspects involved in the combustion of ammonia-hydrogen mixtures (engine performance, combustion indicators and efficiency, NO_x emissions, heat transfer, knock and autonomy) and a comparison with Diesel operation. Finally, the comprehensive set of results proposed hereafter (by the Diesel engine conversion test case) that allows to evaluate the potential of ammonia-hydrogen mixtures cannot be found elsewhere in the existing studies.

The structure of the paper is briefly resumed in the following. After the introduction, the investigated engine and the operating condition (with both Diesel and NH_3–H_2 mixture) are described. The numerical setup of 0D, 1D and 3D simulations is presented. Then results are discussed (both for Diesel and NH_3–H_2 mixtures) and, finally, conclusions are drawn.

2. Engine, investigated conditions and experimental data

2.1. Engine overview, Diesel operating condition and experimental data

The examined engine is a single-cylinder direct-injection 4-stroke engine derived from a larger heavy-duty Diesel unit for marine propulsion applications. The latter is characterized by a maximum specific power $>2000\,kW$, obtained with a total displacement $>50,000 cm^3$. The main characteristics of the single-cylinder engine are reported in Table 2. The engine is equipped with a common rail injection system able to manage injection pressures up to $160\,MPa$ and, due to the solenoid electro-injector, multiple injection strategies can be employed. Diesel is injected at $1550\,bar$ via a centrally mounted 8-holes direct injector. No turbocharger is present. Indeed, an external supercharging system is able to provide intake pressures up to 4 bar and presents a pressure regulation valve which instantly adjusts the flow in order to reach the required pressure value. The engine is connected to an asynchronous motor by a HBM T10FS torsiometer, which allows torque acquisition. In addition, the flow rate supplied to the engine is continuously measured through a flow sensor meter. The in-cylinder pressure is monitored by a Kistler 7061B piezoelectric pressure transducer and the injection current signal to the solenoid is obtained by an amperometric clamp. All the data are acquired by the AVL INDICOM 621. The AVL DiGas 4000 is used for the acquisition of HC, CO and CO2 concentrations and the fuel equivalence ratio. Moreover, compared to Ref. [78], the same instrument (whose main characteristics are summarized in Ref. [79]) is adopted to obtain NO_x concentration at the exhaust.

Table 2 – Main engine features.

Engine Model	Single cylinder Diesel unit
Compression ratio	13.6 : 1
Bore/Stroke, *mm*	170/185
Displaced volume, cm^3	4200
Valve number	2 intake + 2 exhaust
Maximum brake power, *kW*	155
Maximum revving speed, *rpm*	2100

The engine is numerically investigated at part load (93 *kW* as brake power) and 1700 *rpm*. In fact, for this condition, all the data (brake torque, air flow rate, fuel flow rate, boost pressure, in-cylinder pressure and emissions) are available for CFD computations. Boost pressure and inlet temperature provided by the bench for the investigated condition are equal to ~ 2.8 bar and ~ 298 *K*.

2.2. Operation with NH_3–H_2 mixtures

In the present study, the engine operation under NH_3–H_2 mixtures aims at reproducing the original Diesel operation described in the previous paragraph. Hence, nominally, the operating condition is the same. De facto, as it will be evident in the result section, the engine output is slightly different as it is not known, a priori, the exact amount of ammonia and hydrogen required to achieve the original engine performance. In this regard, conversion is made on equal theoretical heat release. As visible in Table 3, which resumes the investigated fuel compositions (along with mixture qualities and required masses), the theoretical energy is kept the same as in the original engine. This is purposely done, as a first attempt, to obtain a brake power as similar as possible to Diesel operation.

Five fuel compositions are preliminary investigated (at $\Phi = 1$), ranging from pure ammonia to pure hydrogen, then the mixture NH_3–H_2 80mol%-20mol% is selected as best compromise and considered for further investigations (such as operation at $\Phi = 0.4$). The choice of a stoichiometric air/fuel ratio for the preliminary investigations is motivated by the combustion-related properties of the ammonia. In particular, LFS at $\Phi = 1$ is strongly lower compared to traditional fuels (even in case of H_2 addition if the latter is moderate). Therefore, as a preliminary step, it is preferred not to further penalize it moving towards lean (or rich) air/fuel ratios.

Different aspects can be noticed from Table 3. Firstly, a strong increase of the H_2 mole percentage does not correspond to an increase equally large of mass percentage, because of the reduced molecular weight. Secondly, the fuel mass required to obtain the same theoretical heat released diminishes increasing the hydrogen content. This is related to the LHV value that, as visible, is extremely higher for H_2. Thirdly, at $\Phi = 1$, the air mass (required to burn the reported fuel amount) is similar for the different fuel compositions. This is due to the energy content (intended as heat released per air mass unit) which does not remarkably change increasing the hydrogen content. This is due, in turn, to the energy content definition (LHV/α_s), in which both LHV and α_s increase with H_2 concentration. A similar trapped air mass target between the cases implies a minimal difference in terms of boost pressure (ranging from ~ 1.7 to ~ 1.8 bar), which is in turn lower than Diesel operation one. Only decreasing the equivalence ratio to 0.4, as shown in Table 3, trapped air augments along with the boost pressure (up to $\sim 3.8\,bar$). As for the air temperature provided by the test bench, it is supposed to be the same as Diesel case, i.e. 298 *K*.

Operation with NH_3–H_2 mixtures implies modifications to the engine layout compared to the original one. Despite the conversion to the e-fuels is virtual, it is intended to minimize interventions, in order to reduce complexity and costs in case of actual realization. Firstly, the injection system is modified.

Table 3 – Investigated fuel compositions.

Fuel	Diesel	NH_3–H_2 100mol%-0mol%	NH_3–H_2 90mol%-10mol%	NH_3–H_2 80mol%-20mol%	NH_3–H_2 80mol%-20mol%	NH_3–H_2 50mol%-50mol%	NH_3–H_2 0mol%-100mol%
NH_3 [*mol%*]		100	90	80	80	50	0
H_2 [*mol%*]		0	10	20	20	50	100
NH_3 [*mass%*]		100	98.7	97.1	97.1	89.5	0
H_2 [*mass%*]		0	1.3	2.9	2.9	10.5	100
Energy [*J*]	17,630	17,630	17,630	17,630	17,630	17,630	17,630
Fuel Mass [*mg*]	410.0	937.8	875.9	810.1	810.1	597.0	145.7
Air Mass [*mg*]	11,840.0	5674.6	5621.6	5565.2	13,913.0	5382.7	4996.1
Total Mass (Air + Fuel) [*mg*]	12,250.0	6612.4	6497.5	6375.3	14,723.1	5979.7	5141.8
LHV [$MJ/\ kg_{Fuel}$]	43.25	18.80	20.13	21.76	21.76	29.53	121.00
Energy Content, $\Phi = 1$ [$MJ/\ kg_{Air}$]	3.015	3.107	3.113	3.120	3.120	3.152	3.529
α_s	14.34	6.05	6.42	6.87	6.87	9.02	34.29
Φ	0.5	1	1	1	0.4	1	1

The original one is replaced by a solution similar to the apparatus proposed by Lhuillier [53], in which ammonia and hydrogen are stored in tanks, port-injected and mixed with air before the intake plenum, where homogeneity is achieved. Following the works proposed by Dinesh and Frigo [21,27], storage pressure for NH_3 and H_2 can be equal to nearly 9 *bar* and 150 *bar*, respectively. As for the first, it is sufficient to keep NH_3 at liquid phase at room temperature. As for the second, the high value is needed to achieve a density sufficient for the engine test at the bench. Lower storage pressure for the hydrogen would lead to a rapid depletion. Geometry of head, liner, piston and ports is preserved, along with the compression ratio. The latter is kept not to penalize the efficiency, relying on anti-knock quality of the ammonia. Diesel injector faced to the combustion chamber is replaced by a commercial spark plug with an electrode gap of 0.8 *mm*. However, for simplicity, the spark plug geometry is not included in the numerical model. As for the electrical circuit, a coil ignition system of a current production high performance engine is considered. The secondary circuit is characterized by resistance, inductance and electric energy equal to 2100 *Ohm*, 1.8 *H* and 44 *mJ*, respectively. As for the valve lifts, they are modified in order to minimize the overlap (wide in the original Diesel version to promote exhaust gas release), thus reducing the possibility of fuel leakage at the exhaust. This is done anticipating the exhaust valve closing (EVC) and retarding the intake valve opening (IVO). In addition, exhaust valve opening (EVO) is delayed in order to maximize the indicated work. De facto, in the exhaust profile, ramps are approached reducing the interval of maximum lift. As for the intake profile, the shortening takes place via a scaling as the interval of maximum lift is too short and approaching the ramps would lead to a reduction of the maximum lift and a consequent reduction of the permeability. This optimization of the valve lifts accounts for only the investigated condition. In a future development of the present work it will be necessary to evaluate the effectiveness of these profiles even on other operating conditions. A comparison between original and modified valve lifts is proposed in Fig. 1.

It is important to point out that the proposed conversion accounts for (most of) the thermo-fluid dynamics aspects. The structural ones are not considered in the present paper, even if they are not of secondary importance. In fact, hydrogen characteristics are able to strongly affect the mechanical strength of components as valves and injectors. This requires the adoption of ad-hoc materials and/or superficial coatings.

3. Numerical set-up

0D, 1D and 3D tools that compose the CFD framework proposed in the present paper are extensively described in the following along with their numerical setup. As anticipated in the introduction, 0D/1D chemical kinetics models are exploited to support 3D simulations via autoignition delay time table. Moreover, they allow insights on different aspects such as laminar flame speed and NO_x emissions. The 1D model of the engine provides 3D simulations with boundary conditions and helps to evaluate the engine performance. 3D in-cylinder analyses estimate combustion efficiency, NO_x emissions, heat transfer and knock.

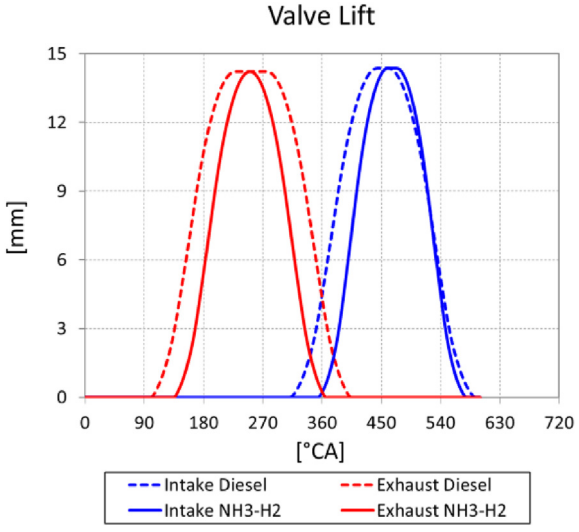

Fig. 1 – Intake and exhaust valve lifts for the original Diesel engine and the modified one.

3.1. 0D/1D chemical kinetics models

Chemical kinetics calculations are exploited to obtain values of ignition delay, laminar flame speed and NO_x concentration. For all the 0D/1D chemical kinetics simulations DARS v2020.1 licensed by SIEMENS PLM is adopted. Different chemical schemes are used based on the specific task. All the 0D/1D analyses are briefly described in the following.

- Ignition delay calculations: they are carried out via a constant pressure 0D (unsteady) reactor. Governing equations for the reactor are widely described in DARS manual [80]. Calculations are performed for different NH_3–H_2 mixtures, 100mol%-0mol%, 90mol%-10mol%, 80mol%-20mol%, 50mol%-50mol% and 0mol%-100mol%. Different chemical schemes are adopted, namely Shrestha [12], Klippenstein [81] and Creck [82–84]. For these mechanisms, the number of species is 125, 33 and 31, while the number of reactions is 1090, 207 and 203, respectively. As for the thermodynamic conditions, wide ranges of pressure and temperature are considered, in order to account for all the possible states experienced by the charge during the hot portion of the engine cycle. In detail, $20 \leq p\ [bar] \leq 200$, $400 \leq T_u\ [K] \leq 1400$, $0.9 \leq \Phi \leq 1$ and $0 \leq \text{EGR}\ [mol\%] \leq 5$. It is useful to point out that the high-temperature auto-ignition delay time is defined as the time for which the mixture temperature increase from its initial state exceeds 400 K [85].
- Laminar flame speed calculations: they are performed adopting the 1D (steady-state) freely propagating flame tool. A freely propagating flame model is a hypothetical model of a planar, unstretched and infinitely large flame front propagating through a premixed medium. Governing equations can be found in DARS manual [86,87]. The same three chemical mechanisms mentioned in the first bullet point are adopted. Simulations are carried out only for the mixture NH_3–H_2 80mol%-20mol% at $\Phi = 1$ and different conditions in terms of pressure and unburnt temperature. The reason to limit the analysis to a unique mixture (both in terms of fuel composition and air/fuel ratio) is that the latter is identified as the most promising one in the present study, as it will be clarified in the next paragraphs. As for the pressure and temperature conditions, they are represented by the 14 points reported in Fig. 2. They can be considered as representative of the conditions experienced by the mixture during the hot portion of the engine cycle, i.e. between 700° and 765° CA (Crank Angle). Laminar flame speed calculations account for the presence of EGR as well, which ranges from 0 mol% to 2mol%.
- Species concentration calculations: similarly to laminar flame speed ones, they are carried out via the 1D (steady-state) freely propagating flame tool. These simulations are focused on the estimation of the mass concentration of NO_x and, besides the same three chemical mechanisms mentioned in the first bullet point (adopted for the NH_3–H_2 mixtures), a further one still provided by the Creck Modeling Group is exploited (adopted for $C_{12}H_{26}$ which replaces Diesel) [88–90]. On the one hand, NO_x calculations are performed with NH_3–H_2 mixtures for rich-to-very-lean mixtures ($\sim 0.1 \leq \Phi \leq 1.2$) and are mainly used to investigate extreme Φ values that inhibit NO_x formation. On the other hand, NO_x calculations with $C_{12}H_{26}$ provide outcomes to be compared with NO Relaxation Approach (NORA) model [91] for validation purposes, as it will be shown in the next paragraphs.

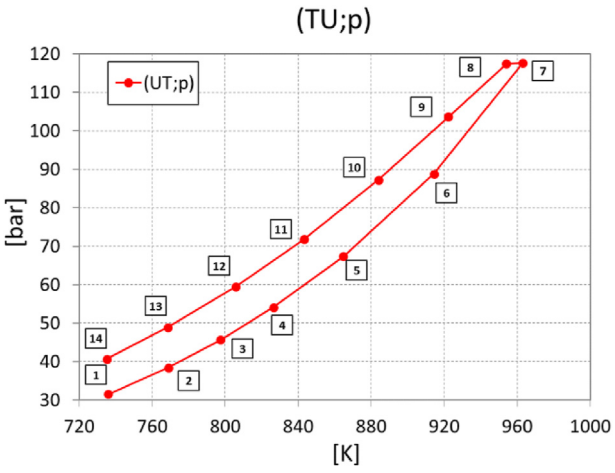

Fig. 2 – 14 thermodynamic states representative of the conditions experienced by the mixture during the hot portion of the engine cycle.

3.2. 1D engine model

GT-SUITE licensed by GAMMA TECHNOLOGIES is the 1D commercial code adopted to represent the engine. The developed model is the same described in Ref. [78] and includes intake and exhaust ports as well as the cylinder. As for the pipes, the unsteady 1D flow is solved, while the in-cylinder phenomena are simulated via a 0D approach. Focusing on Diesel operation, lifts and phasing of the valves correspond to the actual ones and are imposed as inputs to the model. The boosting is not provided by a combination of turbocharger and cooling heat exchanger, but it is simply reproduced imposing the plenum pressure (in order to mimic the bench). Temperature is fixed at the plenum as well. The Woschni-GT model [92] closely resembles the classic Woschni correlation [93] and predicts the convective heat transfer through the combustion chamber walls. Revving speed, injection timing, fuel mass per cycle and plenum pressure are fixed equal to the experimental value; the engine exhaust pressure is set equal to the ambient one. Wall temperatures are fixed equal to the ones adopted in the 3D simulations (that will be presented in the following). Turbulence and combustion are simulated through sub-models available in GT-SUITE. In particular, premixed and diffusive combustion modes of Diesel operation are replicated by the 'DIJET' phenomenological sub-model. The latter is properly calibrated against the experimental data of the investigated condition, adopting a unique set of tuning constants. In particular, the calibration is performed via a tuning of the constants of ignition delay time, jet break-up time, liquid droplet evaporation rate and entrainment rate of air and residuals.

Moving to the NH_3–H_2 mixtures, similarly to Ref. [78], the 1D model of the original Diesel engine is converted to Spark Ignition (SI) operation under NH_3/H_2/air mixtures. Diesel direct injector is replaced by a spark plug. Following the considerations proposed in the previous paragraphs, ammonia and hydrogen are not supplied by port injectors near the combustion chamber but directly imposed at the feeding line of the intake plenum. In particular, the mixture composition (i.e. concentrations of air, NH_3 and H_2) is fixed before the plenum. Valve lifts and phasing are ad-hoc modified, as previously presented. Similarly to the Diesel version, intake pressure and temperature are simply imposed modifying the conditions upstream the intake plenum. In this regard, it is necessary to point out that the mixture temperature corresponds to the one of the air provided by the bench, thus neglecting the effect related to the injection of both H_2 and NH_3. On the exhaust side, ambient conditions are still applied.

Heat transfer model and wall temperatures are the same adopted for the Diesel simulations. As it will be confirmed by the 3D simulations, the total thermal load is nearly the same between Diesel and NH_3–H_2 mixtures (even if differently distributed among the boundaries of the cylinder), so considering the same wall temperatures can be acceptable for the 0D heat transfer model. In-house developed sub-models for turbulence and combustion are implemented into GT-SUITE to perform preliminary simulations aimed at providing boundary conditions for the 3D-CFD analyses.

Turbulence is reproduced by a 0D sub-model, widely validated in the past by the authors [94,95]. Tuning of the turbulence model parameters for the currently investigated engine can be found in Ref. [78]. Briefly, the tuning is realized by a hierarchical 1D/3D numerical methodology, deeply treated in Refs. [78,95–97], where 3D-CFD simulation results of in-cylinder mean flow and turbulence under motored conditions and different speeds are taken as reference to calibrate the user-defined 0D turbulence sub-model.

As for the combustion, similarly to Ref. [78], a predictive sub-model is employed, able to provide accurate results even in presence of limited experimental data or 3D outcomes. It has a physical background relying on a fractal behavior of the wrinkled flame front. De facto, the model reproduces the enhancement of the laminar flame front surface due to the turbulence effect [98]. The laminar flame speed adopted by the model is the same as the one of the 3D-CFD simulations. Therefore, a wide description of the LFS is demanded to the following paragraph.

As previously anticipated, predictive turbulence and combustion models are adopted just in preliminary simulations. In fact, ulterior calculations aimed at verifying the engine output starting from burn rates provided by the 3D-CFD are carried out via a simplified approach based on the application of a combustion profile. In such performance simulations, the heat transfer model is calibrated against 3D outcomes to provide a proper estimation of the heat transfer.

3.3. 3D models

3.3.1. In-cylinder model for Diesel fuel

3D-CFD simulations are carried out with STAR-CD v4.34, licensed by SIEMENS PLM [99]. Turbulence is approached via the $k-\varepsilon$ RNG model for compressible flows [100], widely diffused for in-cylinder simulations in the engine community. The ideal gas equation of state is adopted to close the set of RANS equations. Viscosity, specific heat and thermal conductivity are temperature dependent. The first is modeled by Sutherland equation. The second and the third are polynomial functions. At the walls, a non-slip conditions is imposed and temperature is fixed. Despite intrinsic limitations [101,102], a high-Reynolds (i.e. wall function based) approach is preferred for the near-wall flow modeling, to limit the computational cost. As for the heat transfer modeling, a purposely developed model is adopted, based on a combination of two well-consolidated ones, namely the GruMo-UniMORE (developed by the authors [103–105]) and the Angelberger [106]. As visible in Table 4, the adopted heat transfer model is similar to the Angelberger but with the thermal wall function proper of the GruMo-UniMORE. The reason relies on the opportunity to exploit the capabilities of both the models. In authors' experience [107], Angelberger is recommended when the revving speed is low (especially in SI engines), as in the present analysis. The thermal wall law of the GruMo-UniMORE model, instead, allows to account for the mixture properties thanks to the variable Prandtl number. Therefore, it is possible to account for peculiar characteristics of ammonia and hydrogen. Wall temperatures for head, liner, piston, intake port, exhaust port, intake valve face, intake valve stem, exhaust valve face and exhaust valve stem are fixed to 500 *K*, 450 *K*, 550 *K*, 350 *K*, 550 *K*, 450 *K*, 350 *K*, 810 *K* and 700 *K*, respectively.

Table 4 – Heat transfer models. q_w, ρ, c_p, u_τ, T, T_w, y^+ and Pr are wall heat flux, gas density, gas specific heat, friction velocity, gas temperature, wall temperature, dimensionless distance and Prandtl number, respectively.

GruMo-UniMORE	Angelberger
$q_w = \frac{\rho c_p u_\tau (T - T_w)}{2.075\, ln(y^+) + 13.2\, Pr - 5.34}$	$q_w = \frac{\rho c_p u_\tau T ln\left(\frac{T}{T_w}\right)}{2.075\, ln(y^+) + 3.9}$
Adopted Model	
$q_w = \frac{\rho c_p u_\tau T ln\left(\frac{T}{T_w}\right)}{2.075\, ln(y^+) + 13.2\, Pr - 5.34}$	

PISO solution algorithm and second order MARS numerical scheme are adopted for momentum, temperature and turbulent quantities transport equations. Turbulent Prandtl and Schmidt numbers are constant and set equal to 0.9.

As for Diesel fuel simulations, the computational domain is reported in Fig. 3a) and it includes cylinder and intake/exhaust ports.

The total number of fluid cells is about 475*k* at TDC and 960*k* at BDC. Layer addition and removal is adopted to account for mesh motion. Time step ranges between $1e-6s$ and $1e-7s$, to keep the CFL number below 1. Time dependent pressure and temperature boundary conditions are derived from the GT-SUITE 1D model described in the previous paragraph. As for the spray, a Lagrangian approach is adopted, whose description is demanded to Appendix A,

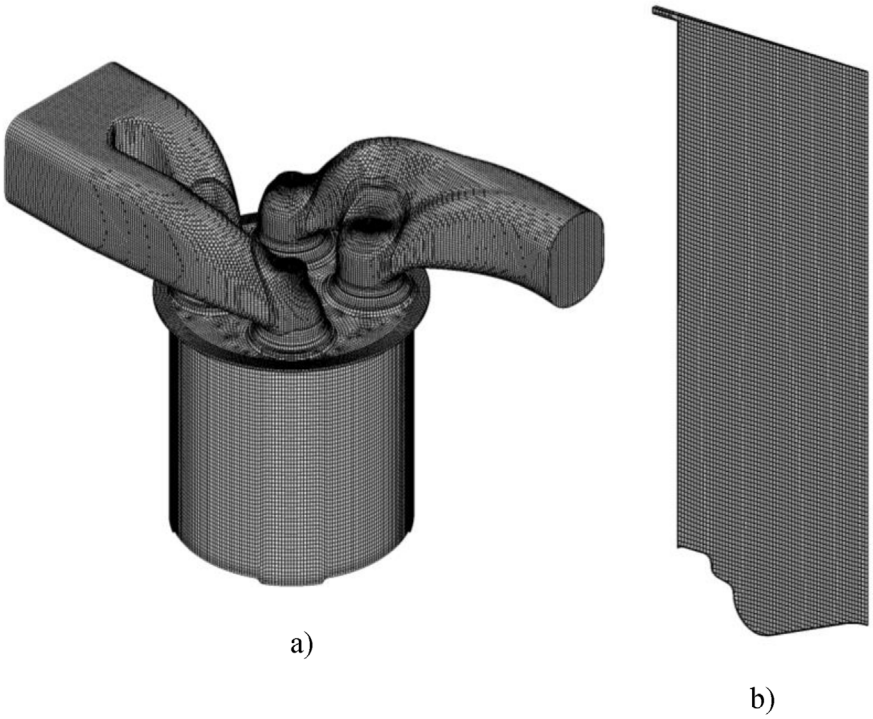

Fig. 3 – Computational grid for a) in-cylinder full chamber simulation and b) in-cylinder sector simulations.

where the vessel spray simulation setup is described and validation is proposed. Senda approach [108] is included to manage the interaction between droplets and walls and the evaluation of the Leidenfrost temperature is demanded to the Habchi model [109].

Combustion is modeled via ECFM-3Z [110], as it was widely validated in previous publications by the authors on several engines [96,104,105,111–113]. ECFM-3Z is a general-purpose combustion model able to simulate turbulent mixing, flame propagation (i.e. premixed or partially premixed combustion), diffusive combustion and pollutant emissions formation. For Diesel combustion simulations in ECFM-3Z, pre-ignition chemical kinetics is not on-line solved: the Tabulated Kinetic Ignition (TKI) model is adopted [114], which relies on pre-computed libraries containing auto-ignition delays. For the present simulations, a table provided with the software installation is adopted, in which delays are computed via DARS using a n-dodecane/p-xylene mixture as Diesel surrogate and a reduced mechanism from LLNL [115]. The same surrogate and mechanism are adopted to compute laminar flame speed (LFS) values which are tabulated as well, similarly to ignition delays, as a function of unburned temperature, pressure, equivalence ratio and EGR.

LFS is exploited in the flame surface density (Σ) transport equation [99] of ECFM-3Z, which governs the turbulent flame propagation (and thus the fuel burning rate) during the first stage characterized by premixed combustion.

Premixed combustion obeys to the one step reaction reported in Eq. (1), in which $C_{12}H_{26}$ (with DF2 properties [116]) is adopted as a representative of the fuel (C_nH_m).

$$\begin{aligned} &C_nH_m + F\left(n+\frac{m}{4}\right)O_2 + (1-F)\left(\frac{n}{2}\right)O_2 \\ &\quad \rightarrow FnCO_2 + (1-F)nCO + F\left(\frac{m}{2}\right)H_2O + (1-F)\left(\frac{m}{2}\right)H_2 \end{aligned} \tag{1}$$

$$F = \begin{cases} 1 & \Phi \leq 1 \\ [4(n+m/4)/\Phi - 2n]/(2n+m) & 1 < \Phi < (2+m/2n) \\ 0 & \Phi \geq (2+m/2n) \end{cases}$$

Considering post-flame reactions, ECFM allows to account for diffusive combustion mode and emission formation.

As for the diffusive combustion, Eq. (1) simplifies to Eq. (2).

$$C_nH_m + \left(n+\frac{m}{4}\right)O_2 \rightarrow nCO_2 + \left(\frac{m}{2}\right)H_2O \tag{2}$$

The fuel burning rate in diffusive mode is calculated via the eddy break-up assumption [99].

As for the emission modeling, NORA [91] and Sectional [117,118] models are activated in order to predict formation of NO_x and soot. As for the unburned hydrocarbons (UHC), there is no specific model and they are simply approximated to the residual fuel at EVO. The presence of unburned fuel can be due to uncomplete premixed combustion or lack of oxygen in the burnt gases (even for a partial oxidation into CO). End of simulation (EoS) is close to the EVO, so that the in-cylinder concentrations of the pollutant emissions at the end of run are adopted for comparison with the experimental data (under the hypothesis that reactions are frozen at EVO). Further details on the methodology to compare emissions from CFD and experiments can be found in Ref. [119].

Simulation start and end are fixed to 90° CA and 810° CA respectively, with 720° CA that corresponds to the TDC of firing. Multiple cycles are run to eliminate the influence of the initial conditions.

3.3.2. *In-cylinder model for NH_3–H_2 mixtures*

Moving to the in-cylinder simulations with NH_3–H_2 mixtures, the computational domain is the same as for Diesel analyses. Wall temperatures and simulation start/end are kept as well. Multiple cycles are run even in this case, to eliminate the effect of the initial conditions. Time dependent pressure and temperature boundary conditions are still derived from the previously described GT-SUITE 1D model. Compared to Diesel simulations where only air flows in the domain from the intake port, a premixed (homogeneous) mixture is fixed as boundary condition at the intake. Besides the proposal of a comprehensive numerical framework, the present paper aims at comparing the operation, on the same engine, with Diesel and NH_3–H_2 mixtures. Therefore, it would be straightforward the adoption of the same numerical framework moving from fossil to e-fuels. This is even more true considering that, for Diesel operation, simulations are validated against experiments, thus the predictive capabilities changing only the fuel should be promising. However, moving from Diesel to NH_3–H_2 mixtures the numerical framework is forcibly different, at least in terms of ignition, combustion and emission modeling. In fact, despite ECFM-3Z and NORA models can simulate all types of combustion (premixed, partially premixed and unpremixed/diffusive), they do not support simulation of fuels devoid of carbon content, as implemented in the adopted STAR-CD version. Conversely, G-Equation and Detailed Chemistry (DC) models (adopted for the simulation of NH_3–H_2 mixtures) cannot simulate diffusive combustion such as under Diesel operation. Apart from ignition, combustion and emissions, the rest of the numerical setup (such as mesh, numerics and turbulence modeling) is the same moving from Diesel to ammonia-hydrogen mixtures.

It is important to point out that, despite experiments are not available in the current work for premixed combustion with NH_3–H_2 mixtures, validation of G-Equation along with the adopted ignition model and the Damköhler (Da) correlation for the turbulent flame speed has already been carried out by the authors at similar conditions: in Ref. [120] a Diesel engine converted to SI operation with hydrogen is investigated and numerical results are successfully validated against experimental data.

As anticipated, in case of NH_3–H_2 mixtures, combustion and emissions formation are simulated via G-Equation [121,122] and DC [99,123,124]. G-Equation is a level-set-method based combustion model, which separates the burnt region from the unburnt one by an iso-surface of a scalar named G. This iso-surface is defined as the $G = 0$ surface. It can be seen that the $G = 0$ iso-surface only defines the flame front position. To describe the flame structure in turbulent flows, the variance of G (G') is also required, from which we can obtain the turbulent flame thickness.

S_T is the turbulent flame speed which is expressed by the Da correlation [122] and reported in Eq. (3).

$$S_T = S_L\left(1 + \cdot A \cdot \left(\frac{u'}{S_L}\right)^n\right) \tag{3}$$

A and n values are inherited from Ref. [99] and are equal to 3.6 and 5/6 respectively. u' is the RMS of the turbulent velocity fluctuations. As visible in Eq. (3), S_T relies on S_L. With respect to Diesel simulations carried out in the present work, where the laminar flame speed is tabulated, for NH_3–H_2 mixtures LFS is obtained via correlations inherited from Ref. [125] and characterized by the form reported in Eq. (4) (unless the scaling factors for the very lean conditions which are omitted here for brevity).

$$S_L = S_{L0}\left(\frac{T_u}{T_{ref}}\right)^{\alpha}\left(\frac{p}{p_{ref}}\right)^{\beta} \tag{4}$$

S_{L0}, α and β are polynomial functions depending on the equivalence ratio. Coefficients for such polynomials (and for the scaling factors at very lean conditions) as well as values of reference pressure (p_{ref}) and temperature (T_{ref}) can be found in Ref. [125]. In this reference, coefficients and reference quantities can be found for LFS of both pure ammonia and pure hydrogen and are obtained via chemical kinetics simulations carried out with DARS software and the Creck mechanism [82,83] already mentioned in the previous paragraphs. It is important to point out that, as visible in Eq. (4), EGR is not accounted for in the laminar flame speed correlations available in Ref. [125]. Nonetheless, they are adopted because EGR percentage (by mass) is nearly 1.7% for all the analyses presented in the following, thus its impact is not significant. This approximation will be further discussed in the results section. Moreover, since the adopted laminar flame speed correlations for ammonia and hydrogen are obtained from 1D chemical kinetics correlations, they do not include the effects of the instabilities due, for example, to differential diffusion, which is non-negligible in case of hydrogen. However, as reported in Refs. [120,126], the inclusion of the instabilities is not essential to obtain a reliable estimation of the engine performance.

In order to obtain laminar flame speed for NH_3–H_2 mixtures, starting from the ones for pure ammonia and pure hydrogen, Hirasawa model [127] is adopted. This model assumes that the flame temperature of each fuel component is determinant to obtain the laminar burning velocity of the mixture. Therefore, the latter (S_{Lm}), reported in Eq. (5), is made of quantities that are weighted composition of the properties of the component fuels.

$$S_{Lm} = e^{-\frac{T_{am}}{T_{fm}}} \tag{5}$$

Definitions of T_{am} and T_{fm} are reported in Eq. (6) and Eq. (7).

$$T_{am} = \frac{-\sum_{i=1}^{n} x_i n_i T_{f,i}\, ln(S_{L,i})}{n_m} \tag{6}$$

$$T_{fm} = \frac{-\sum_{i=1}^{n} x_i n_i T_{f,i}}{n_m} \tag{7}$$

x_i is the mole fraction of fuel component i in the mixture while n_i is the number of total moles of products and inert gases produced from the combustion of 1 mol of fuel

component i under stoichiometric conditions. $T_{f,i}$ and $S_{L,i}$ are flame temperature and laminar burning velocity, respectively, of fuel component i at the equivalence ratio of the mixture. n_m is defined as in Eq. (8).

$$n_m = \sum_{i=1}^{n} x_i n_i \tag{8}$$

In the light of the mixtures investigated in the present study and previously mentioned, x_{NH3} assumes values equal to 0, 0.5, 0.8, 0.9 and 1. x_{H2} values are 0, 0.1, 0.2, 0.5 and 1. n_{NH3} and n_{H2} are equal to 19.28 and 5.76, respectively. Finally, $T_{f,NH3}$ and $T_{f,H2}$ are fixed to 2073.15 K and 2383.15 K [128], which represent adiabatic flame temperatures at ambient conditions, namely 298 K and 1 $bar(a)$. The adoption of fixed values despite conditions change during the engine cycle will be justified in the result section of the present paper.

In order to account for flame quenching at the walls, a dedicated model is adopted [99]. It is based on the calculation of the quenching distance l_q, reported in Eq. (9). When the distance between a cell centroid and a wall is less than l_q, the turbulent flame speed of the cell is set to the laminar flame speed.

$$l_q = f_q\left[11.5\mu_l \Big/ \left(\rho C_\mu^{0.25} k^{0.5}\right)\right] \tag{9}$$

f_q is a parameter whose value is set to 5, as in Ref. [99]. ρ and μ_l are density and molecular viscosity, k is the turbulent kinetic energy and C_μ is the empirical coefficient adopted in the formulation of the turbulent viscosity. 11.5 represents the value of the dimensionless distance (y^+) which should act as separation point between viscous sub-layer and log-region in the boundary layer. De facto, the model establishes that below a y^+ of 57.5 (i.e. in both viscous sub-layer and buffer region) the flame stretch due to turbulence is negligible. This represents a simplification of the Bruneaux model [129]. In fact, the latter provides for a correction of the integral length scale (to be adopted in the stretch effect calculation) approaching the wall, namely for $y^+ < 50$, to account for that vortices larger than their distance to the wall are not expected to survive. In the present model, instead, for $y^+ < 57.5$, turbulence effect on the flame speed is totally neglected.

Despite separation of burnt and unburnt gases is ideally governed by G iso-surface, the presence of a flame brush is considered by means of the definition of a reaction progress variable (c), determined via the turbulent flame brush thickness [99]. Value of c ranges from 1 (unburnt mixture) to 0 (fully burnt mixture).

As stated before, G separates burnt and unburnt regions. When spark occurs and $G = 0$ iso-surface starts propagating, c value diminishes. When the progress variable becomes lower than 0.99, Detailed Chemistry model activates. The latter is designed to meet the requirements of incorporating detailed chemical kinetics in engine simulations. This model efficiently solves transport equations for all the species, in which the production/consumption rate is obtained by means of a detailed reaction mechanism.

DC is purposely adopted to predict emissions formation. For example, considering NO_x, transport equations for NO and NO_2 allow to trace production/consumption of these quantities.

As for the chemical schemes adopted in the 3D in-cylinder simulations with DC, Shrestha, Klippenstein and Creck mechanisms have been considered, that are the same exploited for 0D/1D analyses in DARS.

For the NO_x evaluation, the hypothesis of frozen reactions after EVO is still assumed. Moreover, even in this case, concentration in the cylinder at EoS is considered, despite the latter occurs well before the EVO for NH_3–H_2 mixtures. The reason is that NO_x concentration does not remarkably change after the EoS.

In addition to NO_x, the estimation of unburnt NH_3 and H_2 at the exhaust is possible as well. The two e-fuels that are not consumed contribute to the formation of unburnt NH_3 and H_2 at the exhaust. Similarly to NO_x (and for the same reasons), it is supposed that unburned NH_3 and H_2 at the exhaust can be calculated via the concentrations at EoS.

In order to start the combustion process (imposing an initial flame kernel and governing its growth) and initialize the G-field, an ignition model is adopted.

In order to simplify the modeling of the ignition process, several assumptions are made. First of all, electrical circuit dynamics modeling is not considered for two different reasons. Firstly, the electrical circuit has not a relevant impact on the ignition delay. In fact, as reported in Refs. [130–132], the time interval between nominal spark time and break-down is equal to few microseconds ($\sim 10\mu s$), thus negligible in terms of CA at the currently analyzed revving speeds. Break-down is even faster, thus negligible as well. Secondly, despite a proper modeling of the circuit can help to verify the existence of the conditions for the ignition occurrence, it is not necessary for the present analysis, thanks to the adopted ignition system described in the previous paragraphs, meant to be utilized with SI high performance engines supplied with traditional fuels. In fact, neither the break-down voltage nor the Minimum Ignition Energy (MIE), both able to significantly affect the ignition occurrence, remarkably change moving from fossil fuels to ammonia and hydrogen. Starting from the break-down event, Tambasco [133] shows that addition of methane to air does not remarkably affect the break-down voltage of the latter. Moreover, in Refs. [134–136] it is shown that break-down voltage required by hydrogen is lower than air one. Finally, in Ref. [137] the break-down voltage of ammonia is indicated to be similar to that of air. From this literature review it is possible to conclude that moving from traditional fuels to NH_3–H_2 mixtures should not affect the possibility of break-down to take place.

Focusing on the MIE, it is necessary to anticipate that the NH_3–H_2 mixture selected for the engine operation is the 80mol%-20mol%. For this composition, Verkamp shows in Ref. [11] that MIE is comparable to a traditional fuel such as methane.

As for kernel formation and growth after the spark event, the modeling is inspired to the well diffused Herweg and Maly approach [138] with some simplifications. From Ref. [138], Eq. (10) that governs kernel growth is inherited, where r_k is the kernel radius, ρ_u density of unburned gases, ρ_k and T_k mean density and temperature of the kernel. V_k and A_k are volume and surface of the kernel. S_L and S_{Plasma} are laminar flame speed and expansion velocity of the plasma channel. However, compared to the original version, pressure term

contribution is neglected. Moreover, the turbulent flame speed (S_T) is replaced by the laminar one (S_L). In Ref. [138], a complex expression for the turbulent flame speed is considered, in order to account for that, at very small diameters, S_T has to reduce to S_L (since turbulence is not able to affect the kernel), while at greater values of r_k the impact of turbulence becomes no more negligible.

$$\frac{dr_k}{dt} = \frac{\rho_u}{\rho_k}(S_L + S_{Plasma}) + \frac{V_k}{A_k}\left[\frac{1}{T_k}\frac{dT_k}{dt}\right] \tag{10}$$

In the present case only S_L is considered and the turbulence contribution is neglected. This approximation is justified considering that Eq. (10) is exploited as long as the kernel radius achieves 2 *mm* (after that, ignition model is switched off and only *G*-Equation model acts to govern the burn rate). As reported in Ref. [138], the contribution of the turbulence is significant just beyond radius values of 2 *mm*.

As for S_{Plasma}, it is evaluated as in Herweg and Maly model, i.e. solving a one-dimensional unsteady heat conduction equation as the one reported in Eq. (11).

$$\rho c_p \frac{\partial T}{\partial t} = \frac{\partial}{\partial x}\left(k\frac{\partial T}{\partial x}\right) + S \tag{11}$$

ρ and c_p are density and specific heat, respectively. T and t are temperature and time. x is the coordinate while k and S are thermal conductivity and source term. Compared to Ref. [138], S is neglected, i.e. the power provided by the ignition system is not accounted for. Using as boundary condition (i.e. at $x = 0$, $\forall t$) a temperature of $60 \cdot 10^3$K [138], Eq. (11) investigates the velocity of temperature diffusion along a specific direction starting from a hot point (corresponding to the plasma channel). It is useful to point out that the initial temperature at $x = 0$ is $60 \cdot 10^3$K, while it is equal to the unburnt temperature at $x > 0$.

Since Eq. (10) just describes the kernel growth, an initial value for r_k is required. The latter is adopted equal to $1 \cdot 10^{-4} m$ and the adoption of this value will be further discussed in the results section. It is important to point out that, even if not presented in this paper for brevity, a sensitivity is carried out on the initial r_k value and results do not significantly change if lower values are adopted. Even higher ones can be used without noticeable variations of the combustion indicators, provided that the order of magnitude rests the same as the proposed value (i.e. $10^{-4} m$).

Another important difference compared to Diesel investigation is the inclusion of an in-house developed knock model, adopted to predict abnormal combustion onset for the SI (NH_3–H_2) operations that can potentially limit the performance of the engine. An exhaustive description of the model can be found in Ref. [139] and it will be briefly outlined in the following.

Livengood-Wu relationship [140] reported in Eq. (12) is adopted to detect knock onset.

$$I = \int_{t_0}^{t} \frac{1}{\tau_d} dt \tag{12}$$

t_0 is a conventional time at which the chemical reaction rate becomes relevant for the analyzed case. In this study it is assumed equal to 680° CA, since before this point ignition delays are too high to be relevant for the computation of the Livengood-Wu integral. Time integration in Eq. (12) occurs during the run (t corresponds to the simulation physical time) and, if the condition $I = 1$ is met somewhere in the combustion chamber at a given CA, the latter is defined as the knock onset angle. If the condition is never met, the unburnt mixture is sufficiently knock resistant and autoignition does not occur. The integral function loses any physical meaning for $I > 1$. Therefore, the Livengood-Wu Integral is a synthetic way to model chemical kinetics before knock event, as it is based only on auto-ignition delay times. The main advantages of this approach are: a strong reduction of the computational cost, improvement in the calculation of auto-ignition delays with respect to empirical correlations and, finally, a fully decoupling from the combustion model. The physical variables governing the autoignition delay time (i.e. pressure, temperature, equivalence ratio and EGR) are not related to a specific combustion model.

The knock model is based on an extended set of delays, calculated off-line by a chemical kinetics solver. A description of the chemical kinetics calculations is presented in the previous paragraphs. Delays are used to define a look-up table which is recalled for each fluid cell at every iteration and an autoignition delay is calculated based on the closest physical conditions stored in the look-up table and thanks to a procedure based on multiple linearly interpolating operations. The range of physical conditions (i.e. pressure, temperature, equivalence ratio and EGR) is ad-hoc selected in order to cover all the possible states that the end-gases experience during the hot portion of the engine cycle. The look-up table resolution should be as high as possible, in order to limit the interpolation job and to reduce the related error.

Since the model only aims at tracking knock occurrence, once this condition is met no heat due to autoignition is released and the simulation proceeds as knock did not occur.

Since the number of simulations is large, besides the full chamber, a 1° sector domain is considered as well, to speed up the investigation. This is visible in Fig. 3b) and consists of 2*k* cells at BDC and 1*k* cells at TDC. It is exploited to simulate only the closed-valve portion of the cycle. Wall temperatures are the same as the full-chamber calculations. Initial conditions, at least for the flow field, are mapped from the full-chamber model. Pressure and temperature are fixed as uniform and inherited from GT-SUITE. Mixture composition is uniform as well and obtained from a combination of data reported in Table 3 and GT-SUITE results. Sector simulations are characterized by a single run (a multiple cycle approach is obviously not possible) which starts at 680° CA and terminates at 810° CA.

4. Results

The capabilities of the numerical framework are preliminary assessed on a Diesel operation. As described in the previous paragraph, the setup is not strictly the same moving from Diesel to NH_3–H_2 mixtures: ignition, combustion and emission modeling differ, while the rest is the same. Therefore, aspects such as flow field and numerics can be proficiently validated with Diesel operation. In addition, the latter can be exploited for an assessment of the DC capabilities for the

emissions calculation. In fact, NORA model for the NO_x prediction is validated against experiments, thus it can be used, in turn, as a benchmark for DC. The comparison between DC and NORA is demanded to Appendix B. In this section, after Diesel operation results, the main findings related to the use of ammonia-hydrogen mixtures are presented. Sector geometry is exploited at first, then the results are confirmed on the full chamber, with focus on specific aspects such as heat transfer and emissions. Finally, a deepening on NO_x formation is proposed thanks to both 1D and 3D simulations.

4.1. *Original Diesel engine*

The 3D-CFD in-cylinder simulation is run with the numerical setup described in paragraph 3.3.1 and the validation is carried out against experiments in terms of in-cylinder pressure and emissions. As for the first, numerical and experimental curves are proposed in Fig. 4. As for the latter, comparisons are proposed in Fig. 5a) and 5b). For all the quantities, the agreement between simulations and experiments is satisfying. It is useful to remember that numerical values of NO_x and UHC represents concentrations in the cylinder at the end of run (which is just before the EVO), coherently with the validated methodology proposed by the authors in Ref. [119]. Moreover, on the numerical side, NO_x are only composed by NO, as concentration of NO_2 is negligible.

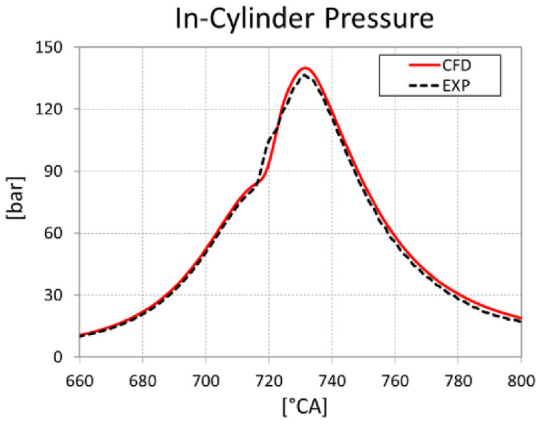

Fig. 4 – Numerical-experimental comparison in terms of in-cylinder pressure.

4.2. *1D chemical kinetics results: analysis of LFS and initial kernel radius*

The first results presented in this section are focused on the laminar flame speed. First of all, the goal is the validation of the Hirasawa formulation for the blending. In fact, as anticipated in the numerical setup description, it relies on (constant) adiabatic flame temperature values inherited from literature for ammonia and hydrogen. Fig. 6 shows the calculated adiabatic flame temperatures (obtained from the LFS simulations) for the thermodynamic states of Fig. 2. With respect to the values adopted in the present paper and reported in figure for comparison, the calculated variable temperatures are much greater. Nonetheless, the impact in the Hirasawa laminar flame speed values is negligible, as demonstrated by Fig. 7 that compares, for the same thermodynamic states, LFS values provided by Hirasawa as adopted in the current work and ones coming from Hirasawa provided with variable adiabatic flame temperatures. Interestingly, LFS results refer to the NH_3–H_2 mixture 80mol%-20mol% as it will be selected, in the following, as the most promising mixture for ICEs.

Still on the validation of the Hirasawa formulation, Fig. 7 reports data (with blue bars) coming from the 1D chemical kinetics simulations carried out with the Creck mechanism. The latter is the one adopted to obtain the laminar flame speed correlations combined by the Hirasawa formulation. Therefore, comparing Hirasawa output with 1D results allows to evaluate the capability of Hirasawa to represent the laminar flame speed of the investigated blend.

Besides the validation of Hirasawa formulation, the data set presented in Fig. 7 with black bars is useful to evaluate the approximation previously declared and dealing with EGR presence in the mixture. As described in the numerical setup, laminar flame speed correlations available in literature and not including EGR are adopted. This is justified by the minimal presence of EGR for the analyzed operations. In Fig. 7, laminar

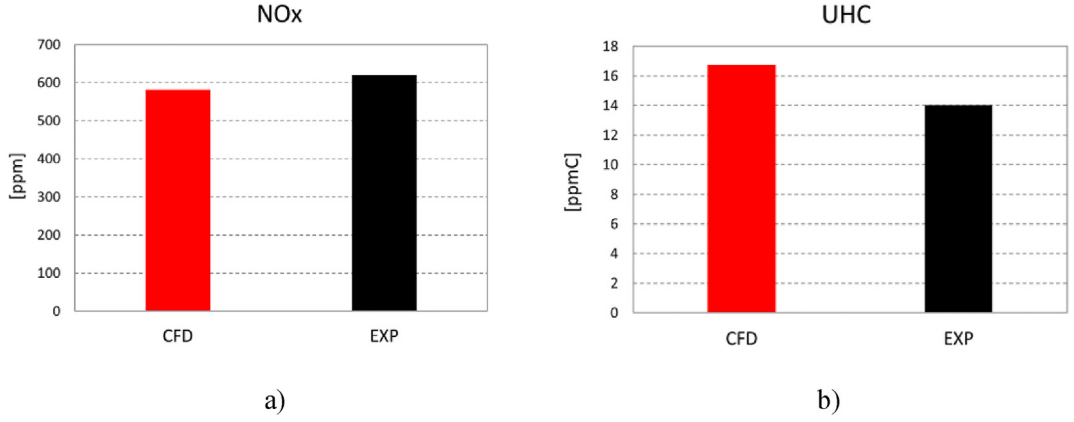

Fig. 5 – Numerical-experimental comparison in terms of exhaust gas emissions: a) show nitrogen oxides and b) unburned hydrocarbons (expressed as *ppmC*, i.e. *ppmC1*).

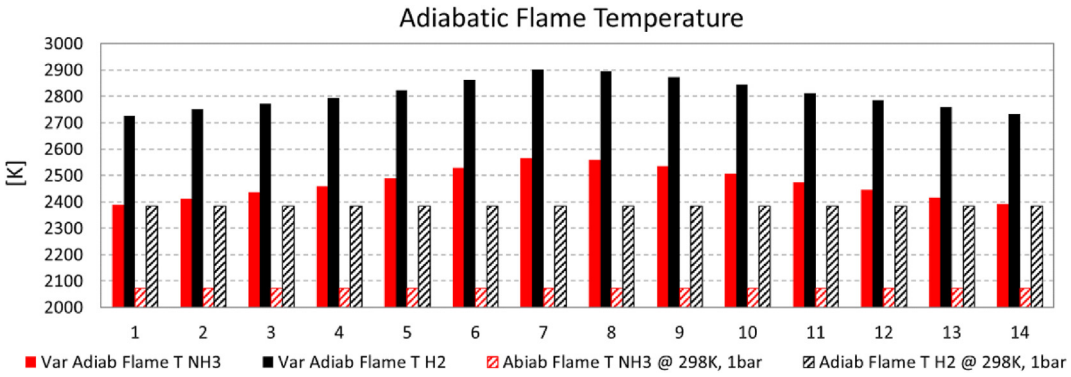

Fig. 6 – Adiabatic flame temperatures for NH_3 and H_2. Both constant values (i.e. fixed at 298 *K* and 1 *bar*) and variable ("Var") ones with the thermodynamic states are reported.

flame speed values obtained with and without EGR are compared (on equal chemical scheme, i.e. the Creck one). As visible, with a 1.7% content by mass of EGR, the reduction of LFS is negligible.

Moving to the analysis of the initial kernel radius, it is useful to remember that the latter is set equal to $1.0 \cdot 10^{-4} m$ in the ignition model adopted in the present paper in case of NH_3–H_2 mixtures. This value or, to be precise, this order of magnitude comes from an estimation of the initial burnt mass volume based on the approach proposed in Ref. [141]. In detail, the initial volume of burnt mass ($V_{k,init}$) is calculated as in Eq. (13), where a cylinder of height equal to the spark gap (d_{gap}) and a radius equal to the flame thickness (δ_L) is considered. The initial radius ($r_{k,init}$) of the adopted spherical kernel is obtain from Eq. (14).

$$V_{k,init} = d_{gap} \pi {\delta_L}^2 \tag{13}$$

$$r_{k,init} = \left(\frac{3}{4\pi} V_{k,init} \right)^{1/3} \tag{14}$$

As for the estimation of δ_L, it is provided by the laminar flame speed calculations carried out in the present work, whose description is proposed in the previous paragraphs. The chemical kinetics calculations are carried out at the state 1 of Fig. 2, with the NH_3–H_2 80mol%-20mol% mixture, by means of the already mentioned mechanisms (namely Shrestha, Klippenstein and Creck) and they provide similar δ_L values, as shown in Fig. 8. State 1 is considered as representative of the conditions at the combustion start and the attention is focused on NH_3–H_2 80mol%-20mol% mixture for the same reasons described above in the paragraph. Besides thickness, Fig. 8 reports the corresponding $r_{k,init}$ values, for a spark gap of 0.8 *mm*. The initial kernel radius is almost the same for the different schemes (similarly to the thickness) and the values justify the order of magnitude adopted in the present ignition model.

4.3. *Preliminary 3D results with NH_3–H_2 mixtures (sector simulations)*

The first set of analyses is carried out with the 1D engine model, just to obtain the boundary conditions (not reported for brevity) for the 3D simulations. In order to match the target masses of air and fuel reported in Table 3, pressure at the boundary of the intake plenum is reduced compared to Diesel

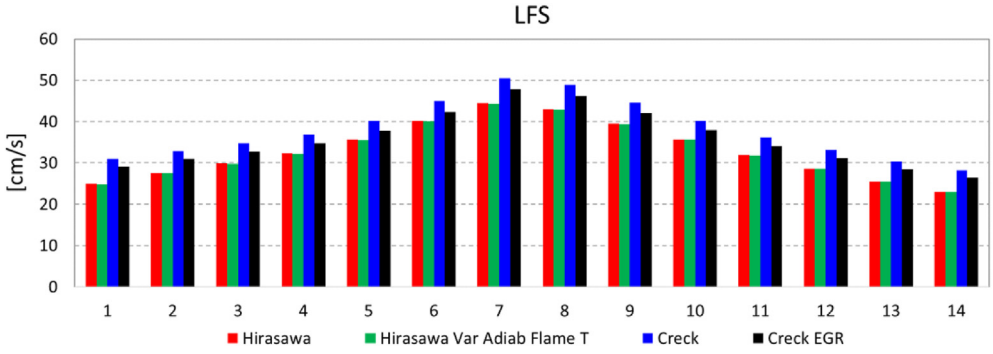

Fig. 7 – Laminar flame speed values for the NH_3–H_2 mixture 80mol%-20mol% and different thermodynamic states. Red bars indicate values obtained by Hirasawa formulation and constant adiabatic flame temperatures, while green bars still come from the Hirasawa formulation but the adopted adiabatic flame temperatures are variable ("Var") with the thermodynamic state. Blu and black bars report values obtained with chemical kinetics simulations, but LFS values given by black bars also consider the presence of 1.7% by mass of EGR in the mixture. (For interpretation of the references to colour in this figure legend, the reader is referred to the Web version of this article.)

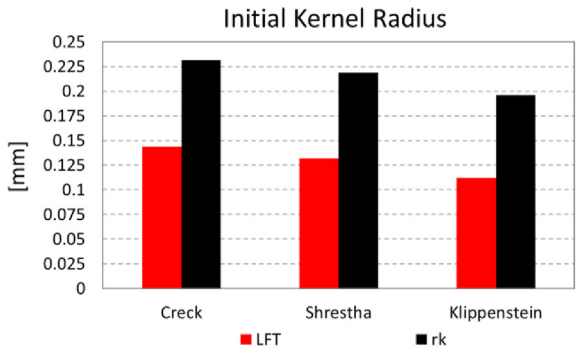

Fig. 8 – Laminar Flame Thickness (LFT) and initial kernel radius values for different chemical schemes.

operation and ad-hoc tuned, case-by-case. An important outcome of the 1D preliminary simulations is that the resulting (internal) EGR is similar for all the investigated fuel mixtures and equal to ~ 1.7% (by mass and calculated as mass of burnt gases over the total mass of the cylinder). Pressure and temperature time-dependent boundary conditions for the 3D model are extracted for the NH_3–H_2 mixture 100mol %-0mol%. For the same fuel composition, a preparatory 3D full chamber simulation is run (with the numerical setup described in paragraph 3.3.2) to obtain initial conditions for the sector domain. The latter is exploited to carry out 3D analyses aiming at individuating the best NH_3–H_2, simultaneously minimizing the computational effort. The full chamber simulation provides flow field and turbulent quantities (k and ε) that are mapped on the sector mesh, while pressure and temperature are uniform in space and inherited by the 1D model. As for the composition, it is calculated considering the mixture qualities reported in Table 3 and adding 1.7% (by mass) of EGR as indicated by GT-SUITE. De facto, the adopted composition roughly corresponds to the 1D one. As stated above, the EGR fraction is similar for all the investigated mixtures and equal to nearly 1.7% by mass. Hence, this value is adopted for all the cases without committing a significant error. It is important to point out that initial flow and turbulent fields are kept for all the mixtures as well. This is a stronger approximation compared to EGR fraction. However, this is done for multiple reasons. Firstly, to reduce the computational effort, otherwise an initial full chamber simulation would be required for each investigated NH_3–H_2 mixture. Secondly, intake pressure is similar, in fact the involved total masses shown in Table 3 are similar for the NH_3–H_2 mixture cases at $\Phi = 1$. Therefore, it is expected that even flow and turbulence fields are similar for the different mixtures. Thirdly, the comparison between the mixtures is even more robust if the only difference between the cases consists only in the mixture itself.

In order to save the computational cost, in the sector simulations (run with the numerical setup described in paragraph 3.3.2) only a single chemical mechanism (Shrestha one) is considered to compute NO_x via DC. A sensitivity to the mechanism will be proposed in the full-chamber simulations.

Fig. 9a) to 9e) show the in-cylinder pressure for different NH_3–H_2 mixtures and spark timings. As for the spark timings, the selection provides for starting at 720° CA, progressively anticipating with a step of 5° CA. The end value is determined by performance or knock. For NH_3–H_2 mixtures 100mol %-0mol%, 90mol%-10mol% and 80mol%-20mol%, the most anticipated timing is 700° CA as moving from 705° CA to 700° CA a decrease of performance is noticed, as reported in Fig. 10 where the gross Indicated Mean Effective Pressure (IMEP) is shown for the cases. Instead, for NH_3–H_2 mixtures 50mol %-50mol%, the most advanced spark timing is determined by the knock onset. In this regard, Fig. 11a) and 11b) show the flame front position which defines the end gas region and the value of the Livengood-Wu integral at 730° CA, for the spark timing of 705° CA. In the end gas, the integral overcomes the threshold value of 1, which means that auto-ignition conditions are met. It is interesting to point out two different aspects. Firstly, in order to better define the Maximum Brake Torque (MBT), in proximity of the most advanced timing (limited by performance or knock) stepping is refined to 2.5° CA. Secondly, for the knock occurrence individuation, the approach developed in the past by the author is adopted [139]: the end gas is defined at first, considering all the amount of mixture with a progress variable higher than 0.5 (remembering that 1 means unburnt mixture while 0 complete combustion); then, only in that region, Livengood-Wu integral is evaluated and, in case of values higher than 1, knock is detected. The exception compared to the previous mixtures is represented by the pure hydrogen case. In fact, even the most delayed spark timing adopted for the previous mixtures (namely 720° CA) leads to knock onset, as shown by Fig. 11c) and d). Therefore, just in this case, more delayed spark timings are tested. From 720° CA, the spark is delayed with a stepping of 5° CA. Since moving from 725° CA to 730° CA a reduction of performance is already noticed, no further spark timing is tested. Only a refinement of the stepping is considered to test 722.5° CA, which is found to be knock free.

Focusing on Fig. 10 and remembering that all the cases are on equal energy content and Φ, it is interesting to notice that, increasing the hydrogen percentage, the maximum achievable performance (i.e. the maximum gross IMEP) degrades. In addition, the risk of knock increases as well, which further penalize the performance. For example, in case of 100% hydrogen operation, knock onset prevent the possibility to achieve the MBT. Among the investigated mixtures, up to the 50% by mole of hydrogen content it is possible to recover the performance of the original Diesel engine. In case of NH_3–H_2 mixture 0mol%-100mol%, even with the most advanced spark timing allowed by knock, the original performance of Diesel engine is not achieved.

For completeness, Fig. 12 proposes a comparison in terms of combustion indicators. For a proper comparison, results refer to the same spark timing, namely 710° CA. Since pure hydrogen has no spark timing in common with other tested mixtures because of knock onset, it is not included in the comparison. The greater the hydrogen content is, the faster the combustion results. In fact, both Mass Fraction Burnt (MFB) 10% and MFB 50% reduce increasing the presence of H_2. Only MFB 10% ÷ 90% does not present the same behavior, it being nearly constant for the different mixtures. The reason is not related to the chemistry of the fuel, rather to the geometry

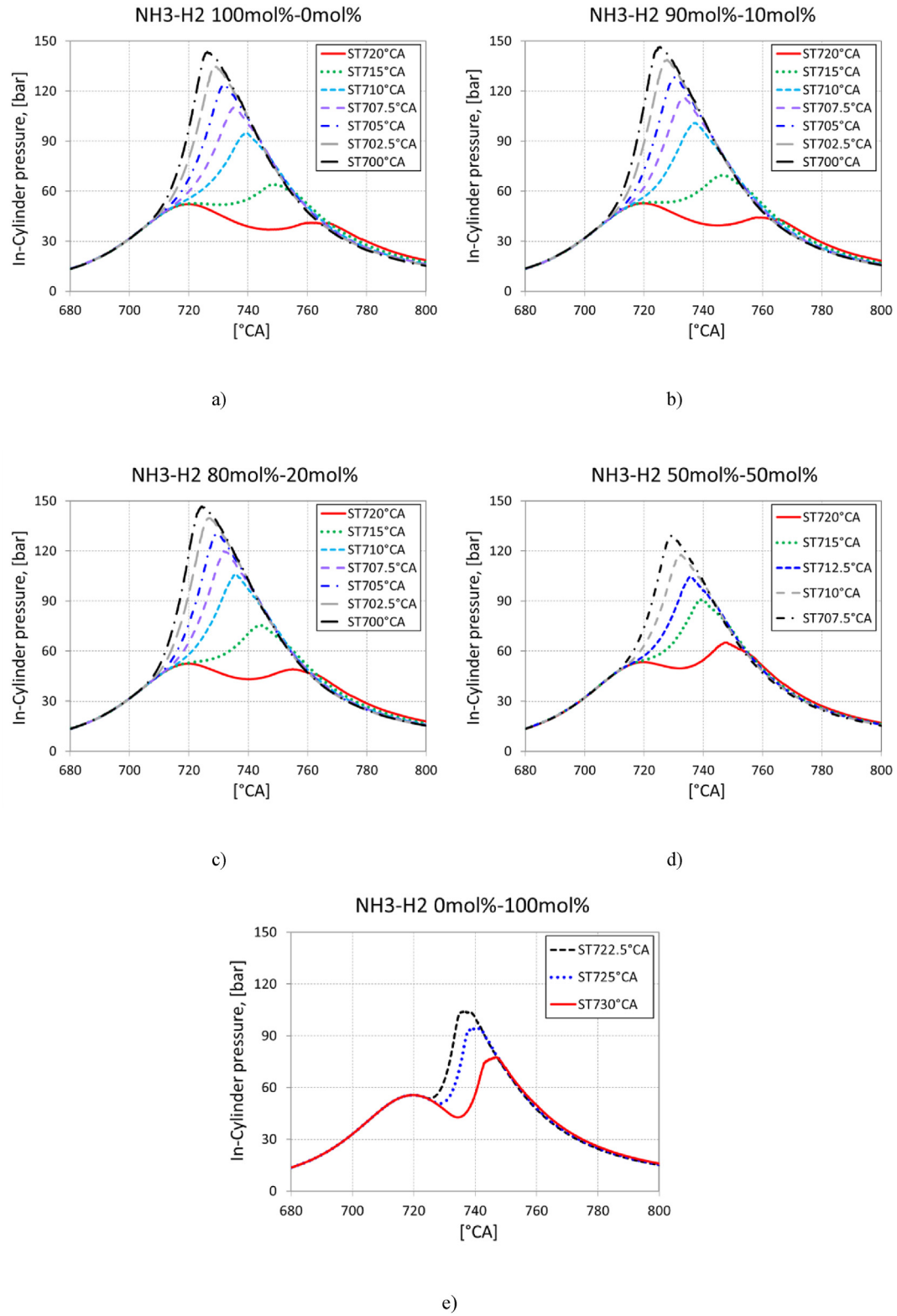

Fig. 9 – In-cylinder pressure traces for different NH_3–H_2 mixtures and spark timings.

of the combustion chamber. In fact, moving to the 90% of burnt fuel, the flame propagates in the squish zone and then approaches the crevice in correspondence of the gasket. Both squish zone and crevice slow down the flame propagation and this effect is more pronounced when the combustion takes place in proximity of the TDC, which occurs in case of high H_2 content as the combustion is more rapid (at least at the beginning).

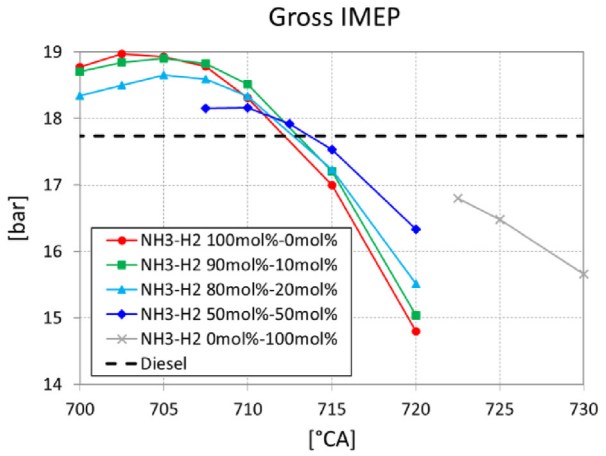

Fig. 10 – Gross IMEP for different NH_3–H_2 mixtures and spark timings.

It is useful to point out two different aspects. Firstly, comparisons of performance between the different fuels are carried out in terms of gross IMEP, calculated as difference between IMEP and PMEP, the latter being the Pumping Mean Effective Pressure. In fact, the actual test bench of the Diesel engine as well as the virtual one for NH_3–H_2 mixtures directly provide the boost pressure required for the engine operation and no turbocharger is included in the hardware. Therefore, in order to avoid the misleading impact of the externally provided boost on the engine performance, the gross IMEP is exploited. Secondly, gross IMEP values (proposed in Fig. 10 and in the following) are obtained from the GT-SUITE model, in which the predictive 0D combustion model is replaced by the imposition of combustion profiles inherited from the 3D sector analyses (and the heat transfer model calibrated ad-hoc to match the 3D outcomes). The adoption of the 1D tool is mandatory to obtain the gross IMEP, as the reduced simulation interval (680°÷810° CA) of the sector simulations is not sufficient to provide the values.

Since the inlet temperature provided by the bench during the tests is low compared to the one expected in a possible actual use of the engine (where it depends on the efficiency of the intercooler), a sensitivity to this parameter is carried out to check the capabilities of the engine to guarantee a knock-free operation. The sensitivity is reported in Appendix C. Despite the overview on the possible combinations of ammonia and hydrogen (included the extreme cases of pure ammonia and pure hydrogen), not all of them can be considered as promising. First of all, pure ammonia and pure hydrogen cannot be taken into account. Both suffer the problems described in the introduction. In addition, pure hydrogen is characterized by strong limitations in terms of performance at $\Phi = 1$, mostly due to knock, as highlighted by the results presented above. This is a confirmation that the high RON number mentioned in the introduction is not sufficient to avoid knock occurrence. As reported in Ref. [142], probably MON (equal to 60 [143]) is a more accurate measure of resistance to knock in hydrogen engines. Focusing on NH_3–H_2 mixtures, low hydrogen content is preferable for the following reasons:

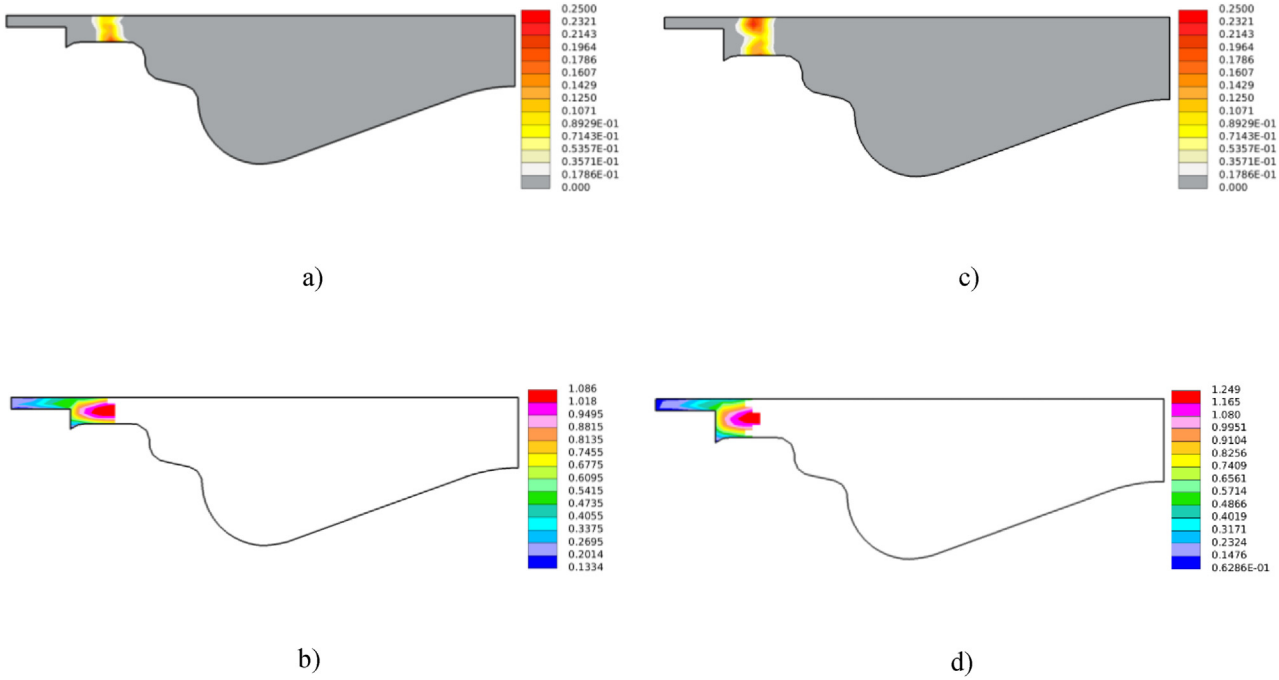

Fig. 11 – a) $c\cdot(1-c)$ field, where c is the progress variable. This allows not only to individuate the flame front position (as an alternative to $G = 0$ iso-surface), but also the entire reaction zone; b) Livengood-Wu integral field, shown for cells whose progress variable is lower than 0.5; c) and b) are similar to a) and b), respectively. Differences are that a) and b) are captured at 730° CA for a NH_3–H_2 mixture 50mol%-50mol% and a spark timing of 705° CA, while c) and d) are taken at 735° CA for a NH_3–H_2 mixture 0mol%-100mol% and a spark timing of 720° CA.

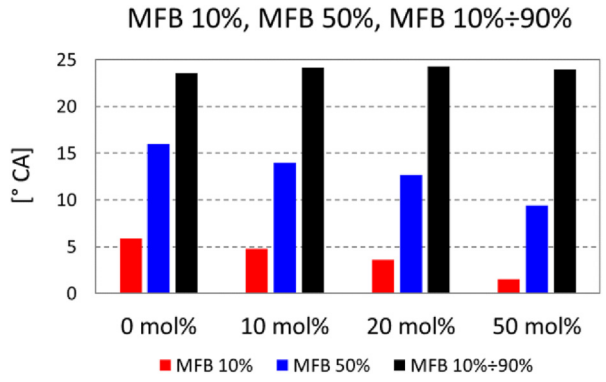

Fig. 12 – Mass Fraction Burnt (MFB) 10%, MFB 50% and combustion duration (MFB 10% ÷ 90%) for different mixtures are reported. In the x-axis, for brevity, the mixture 0 mol% corresponds to the NH_3–H_2 100mol%-0mol %, 10 mol% to the NH_3–H_2 90mol%-10mol% and similarly for the others. Reported values for the mixtures refer to the same spark timing (namely 710° CA). MFB 10% represents the interval between spark timing and 10% of burnt fuel (and similarly for the MFB 50%). MFB 10% ÷ 90% is the interval between 10% and 90% of burnt fuel.

- the problems of autonomy (further discussed in Appendix D with an example) are reduced, even if still remarkable compared to Diesel operation;
- an hydrogen content of 20% by mole is enough, at $\Phi = 1$, to reduce the Coefficient Of Variation (COV) of the IMEP and thus the risk of potential problems such as misfire [20,21,49,53,57];
- as indicated by Verkamp [11], an hydrogen content at least of 20% by mole is needed to lower the MIE of the mixture (compared to pure NH_3) down to a value comparable to the one of a commonly adopted fossil fuel. This is an important aspect in order to ensure the ignitability of the mixture with a standard ignition system of a SI engine;
- finally, limiting the hydrogen content to 20% by mole allows to maintain both quenching distance and MIE sufficiently high compared to H_2 (i.e., once again, comparable to traditional fuels such as gasoline) [11]. This reduces the risk of backfire compared to pure hydrogen (for which direct injection is usually necessary), opening the possibility to port injection.

For these reasons, the NH_3–H_2 80mol%-20mol% mixture is preferred to other fuel compositions. The main drawback related to the use of such a mixture consists in the laminar flame speed value. Fig. 13 shows a comparison between LFS values calculated for the different mixtures at the thermodynamic states of Fig. 2. For comparison, gasoline LFS values are reported as well. As for the mixtures, data are provided by the correlations adopted for the in-cylinder simulations blended with the Hirasawa rule. As for the gasoline, values are provided by the correlation proposed in Ref. [144] for an E0 (that is pure gasoline without ethanol content). The NH_3–H_2 mixture 80mol %-20mol% shows LFS values just slightly higher than pure ammonia and remarkably lower than gasoline. Nonetheless, the presented in-cylinder simulation results demonstrate that, despite the reduced laminar flame speed, the engine is able to obtain the original performance. In addition, to achieve a LFS comparable to the gasoline one, a mole percentage of hydrogen greater than 50% is required. However, this would be detrimental in terms of autonomy, backfire and knock. As shown before, auto-ignition in the end-gases is already detected with a mole concentration of 50% for advanced spark timings and increasing the H_2 content could impede to achieve the original performance.

4.4. *3D results with NH_3–H_2 80mol%-20mol% mixture (full chamber simulations)*

After a cautious screening of the most promising NH_3–H_2 mixture, the capabilities of the latter are verified on the full-chamber domain, where full cycle simulations are run with the numerical setup described in paragraph 3.3.2. Different chemical mechanisms are tested, namely Creck, Shrestha and Klippenstein to test the sensitivity of the results to the mechanism. The selection of the three schemes cited above is carried out considering that all of them account for both NH_3 and H_2 oxidation and include mechanisms of formation and reduction of NO_x. Before the results discussion, it is useful to point out that outcomes presented in the following are characterized by the same laminar flame speed fitting polynomial

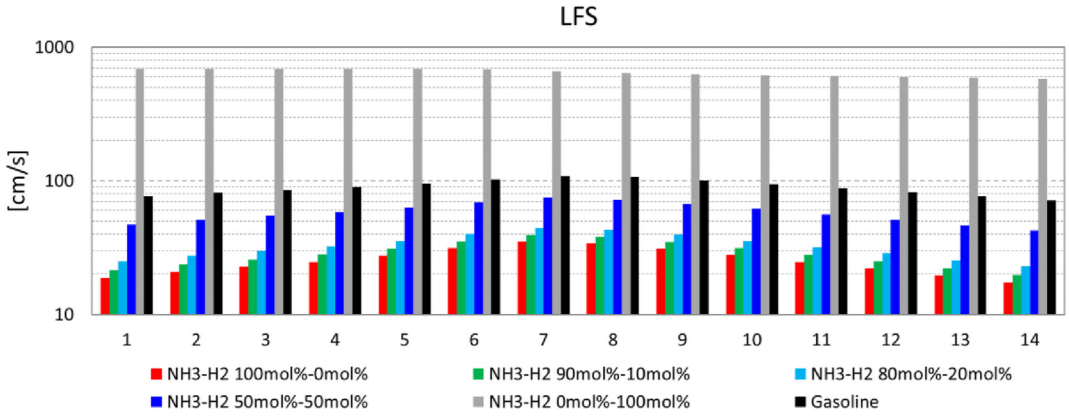

Fig. 13 – Laminar flame speed values provided by correlations for different fuels.

(the one presented in the numerical setup description and derived from the Creck mechanism), since no formulation is available in literature (limited to the authors knowledge) from Shrestha and Klippenstein schemes able to work at the conditions of Fig. 2. In the light of these considerations, it is straightforward that only Creck case is fully coherent, as all the chemical aspects (LFS, auto-ignition delays and NO_x) are calculated via a unique scheme. As for the other cases, despite LFS is inherited from the Creck one as it is common, a dedicated approach is adopted for auto-ignition delay times and NO_x. For example, Shrestha case is characterized by a table of auto-ignition delay times obtained by means of Shrestha scheme and the latter is also employed in the DC model for the nitrogen oxides prediction in the burnt gases. The same is valid for Klippenstein case.

The setup adopted in the full-chamber analyses is inherited from the best case indicated by the sector simulations. Hence, besides the adoption of the NH_3–H_2 mixture 80mol%-20mol%, the spark timing equal to 705° CA and corresponding to the MBT is utilized. As for the boundary conditions, the 1D model whose result in terms of gross IMEP was presented in the previous paragraph and characterized by the imposition of a combustion profile coming from the 3D sector simulation with spark at 705° CA is exploited.

Fig. 14 shows the in-cylinder pressure for Shrestha mechanism. The outcomes by the other schemes are omitted for brevity as nearly coincident. Sector results are included for comparison. The differences between the computational domains (on equal setup) are acceptable even if not negligible and are due to the approximations intrinsic to the sector-based approach. Such differences are then minimized with a slight modification of the spark timing. Anticipating of 1.5° CA, it is possible to obtain almost overlapping pressure traces, thus the full chamber simulations endorse sector results and this is furtherly confirmed by the gross IMEP reported in Fig. 15. In the latter, besides sector results reported for comparison, data relative to the full-chamber simulations are shown, for both the tested spark timings. Similarly to Fig. 14, also in Fig. 15 only full chamber results obtained by Shrestha scheme are reported, as the other mechanisms provide almost the same values. Gross IMEP is similar between the two computational domains and, for both, the performance is higher than the original Diesel engine. Even in this case, gross IMEP values are obtained from the GT-SUITE model via the imposition of the combustion profiles provided by the 3D simulations.

The case represented by the red line in Fig. 14 along with the homologous ones carried out by means of the other mechanisms (not reported for brevity) will be used in the following to investigate the impact of the chemical schemes on knock and NO_x, on equal performance.

Focusing on knock, a comparison between the mechanisms is shown in Fig. 16a) to 16c), in terms of Livengood-Wu integral. The adopted schemes agree in predicting that the analyzed condition is free of abnormal combustion onset. More in detail, Shrestha and Creck provide similar results, while Klippenstein shows lower reactivity, that is Livengood-Wu integral values are lower and end gases are less prone to auto-ignition.

In Fig. 16a)–16c) slight differences can be noticed in the azimuthal direction near the flame front, due to the effect of the hot exhaust valve faces that heat the mixture and lead to higher values of the Livengood-Wu integral on the exhaust side. Nonetheless, the integral is characterized by a very uniform field in the periphery of the combustion chamber. This is due to the homogeneous mixture fraction as well as to the uniform propagation of the flame front visible in Fig. 17a). The latter is in turn caused by the homogeneous mixture itself and the (nearly) axisymmetric flow field. In this regard, the mean velocity vector and turbulent kinetic energy fields are reported in Fig. 17b) and c), respectively, and both are axisymmetric.

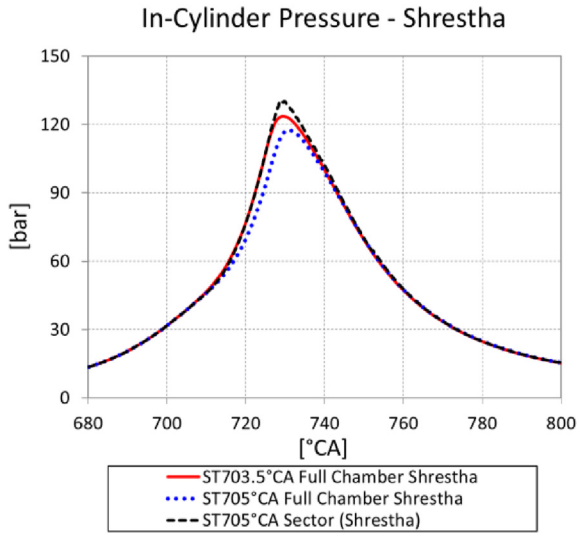

Fig. 14 – In-cylinder pressure curves obtained via full-chamber simulations and Shrestha chemical mechanism. The results deal with the NH_3–H_2 80mol%-20mol% mixture and different spark timings. For comparison, the result obtained with the sector domain is reported.

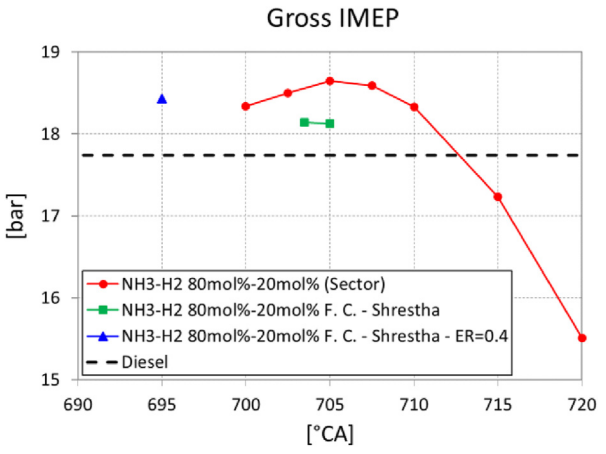

Fig. 15 – Gross IMEP values for both sector and full-chamber (F. C.), obtained with the NH_3–H_2 80mol%-20mol% mixture, Shrestha mechanisms and different spark timings are shown. Results with an equivalence ratio of 0.4 are also reported. Diesel case gross IMEP is included for comparison.

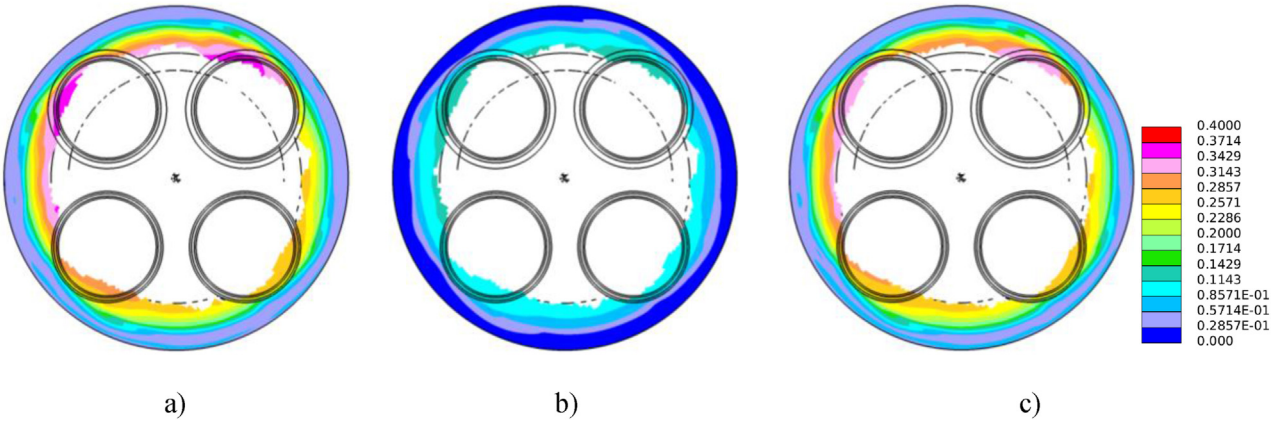

Fig. 16 – Comparison in terms of Livengood-Wu integral between different mechanisms providing the ignition delays: a) Shrestha, b) Klippenstein and c) Creck. All the images report values at 730° CA on a section orthogonal to the cylinder axis and located 2 *mm* below the cylinder head.

Moving to the emissions, the attention focuses firstly on the NO_x. In Fig. 18a) and 18b) (as well as in the following of the paper) only NO is considered, as the production of NO_2 is at least one order of magnitude lower. Results are proposed both in terms of ppm and g/kWh. As for the latter, the values are obtained via the NO mass in the cylinder at the end of the cycle and the engine performance (brake power) provided by GT-SUITE. NO estimation in case of NH_3–H_2 mixtures changes based on the adopted schemes, but all of them agree in predicting a NO concentration higher than Diesel operation. Such increase is less evident in terms of g/kWh as the difference in terms of concentration is a bit dampened by the very different mass between Diesel and NH_3–H_2 mixture cases.

Besides NO, simulations offer the possibility to estimate the unburned NH_3 (UNH_3) and H_2 (UH_2) at the EoS. NH_3 evaluation at the exhaust is crucial as it is dangerous for the human health and, in fact, it is regulated by Euro 7. Results are proposed in Fig. 19a) and 19b), both in terms of ppm and g/kWh. Even for this pollutant, values expressed in g/kWh are calculated via NH_3 and H_2 mass in the cylinder and the engine output provided by GT-SUITE. Results reveal a strong increase of unburnt fuel moving from Diesel to NH_3–H_2 mixtures. Similarly to NO, such increase is less evident in terms of g/kWh as the difference in terms of concentration is dampened by the very different mass between Diesel and NH_3–H_2 mixture cases. One reason for the increase of the unburnt fuel compared to Diesel operation is related to the quenching effect that the flame undergoes approaching the crevice between liner and head (in correspondence of the gasket). This is evident in Fig. 20, which shows the unburned fuel (NH_3+H_2). However, the main reason of the unburnt fuel increase is related to the presence of hydrogen. The unburnt fuel is, in fact, mainly composed by UH_2 which has low concentration but it is diffused everywhere in the chamber and not only in the crevice. The relevant amount of air required by H_2 along with the stoichiometric condition can probably explain the difficulty of the hydrogen to oxidize, but further investigations are left to a future work for a deeper understanding of the phenomenon. By the way, the presence of a non-negligible amount of UH_2 behind the flame is confirmed by the 1D LFS

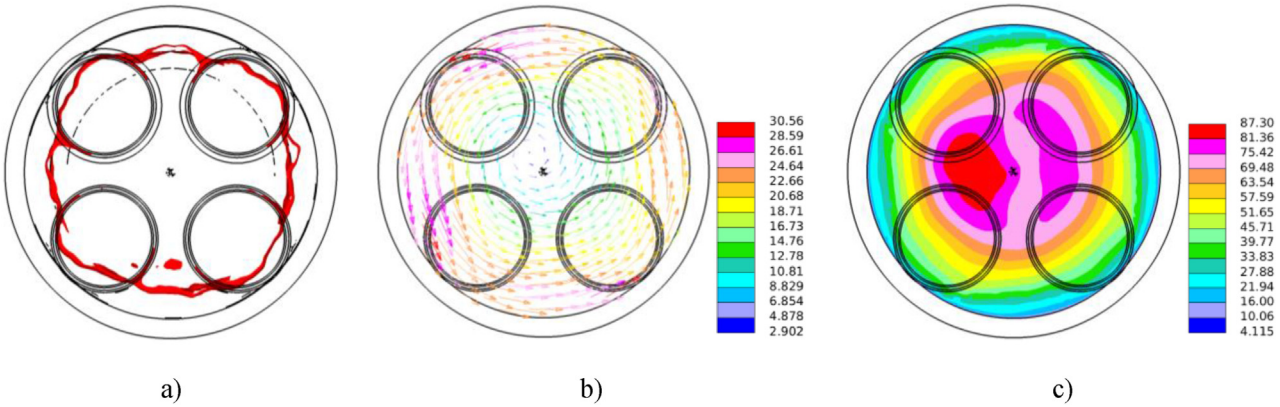

Fig. 17 – a) shows the G = 0 isosurface, providing the flame front position; b) and c) report velocity vectors (with the scale in [m/s]) and turbulent kinetic energy (with scale in [m^2/s^2]). All the images show values at 730° CA on a section orthogonal to the cylinder axis and located 2 *mm* below the cylinder head.

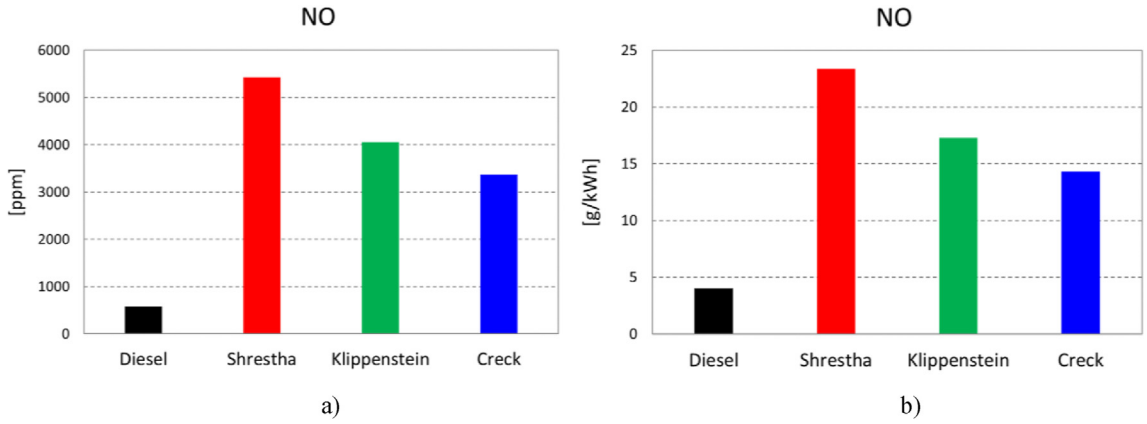

Fig. 18 – NO comparison between Diesel and NH_3–H_2 mixture. For the latter, results from different schemes are proposed; a) show values in ppm while b) in *g/kWh*.

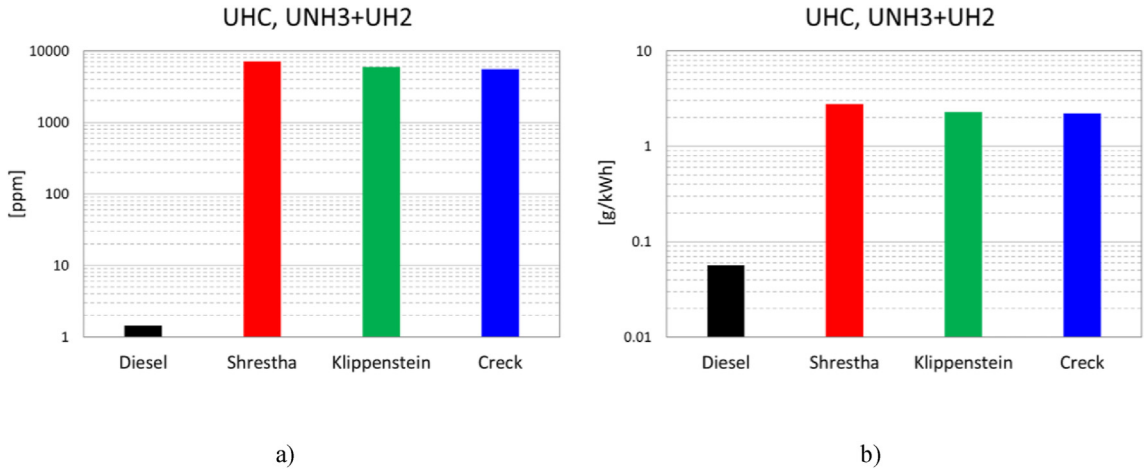

Fig. 19 – Comparison between Diesel and NH_3–H_2 mixture in terms of unburnt NH_3 and H_2. Results for the NH_3–H_2 mixtures are reported for different chemical mechanisms; a) shows values in ppm (also for the Diesel case, unlike Fig. 5b) where *ppmC* is used) while b) in *g/kWh*.

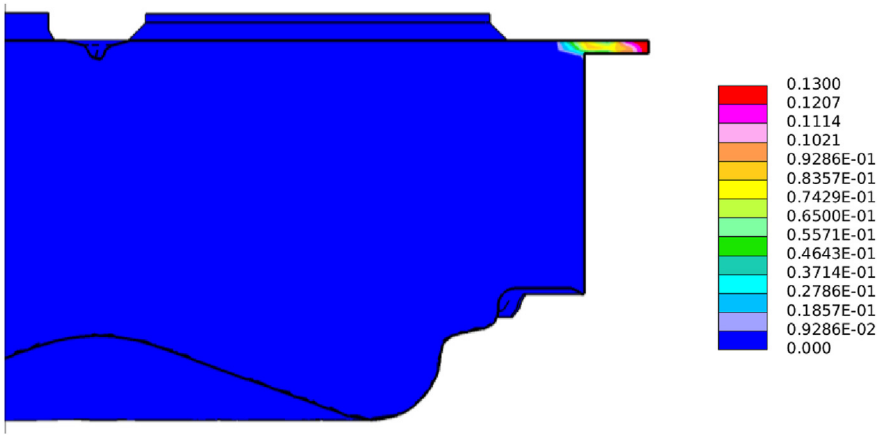

Fig. 20 – Unburned fuel (NH_3+H_2) mass fraction at 770° CA for the Shrestha mechanism case.

simulations (whose results are proposed in Fig. 7 with blue and black bars).

The trend between the schemes is similar to the one of NO, that is g/kWh decrease moving from Shrestha to Creck. Moreover, for both NO and unburnt NH_3–H_2 mixture, Shrestha is the scheme showing higher values compared to the other ones. Such a correspondence between nitrogen oxides and unburnt NH_3–H_2 mixture is not casual, in fact, where UNH_3 and UH_2 are higher, there is more oxygen available for NO formation.

Despite experimental data in terms of emissions are not available for the present study, values obtained in terms of NO_x and UNH_3+UH_2 are coherent with the existing literature [10,20,25,27,48,49,52,53,55,71].

The last aspect investigated is the heat transfer. For the NH_3–H_2 mixture, only results provided by the Shrestha mechanism are shown for brevity. Differences compared to the other schemes are negligible. Results on the main boundaries of the combustion chamber (namely dome, piston and liner) are reported in Figs. 21 and 22 in terms of both instantaneous heat transfer during the hot portion of the cycle and cycle-averaged one. Figs. 21 and 22 reveal that, despite the total cycle-averaged heat transfer (sum on the boundaries) is similar between the cases, the instantaneous distribution is different. In addition, the distribution between the different boundaries changes. Because of the change in the combustion mode, the piston is no more invested by hot jets and the heat transfer on it decreases moving to the NH_3–H_2 mixture. Conversely, because of the (uniform) flame propagation on each direction up to the near-wall region, heat transfer increases on the other boundaries (dome and liner) with ammonia and hydrogen. Concluding, the thermal stress on the components changes even if the total heat rejected to the coolant remains comparable between the different fuels.

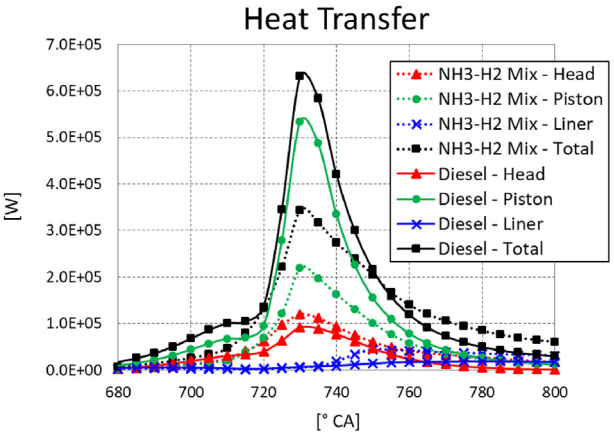

Fig. 21 – Instantaneous heat transfer during combustion on the main boundaries facing the chamber.

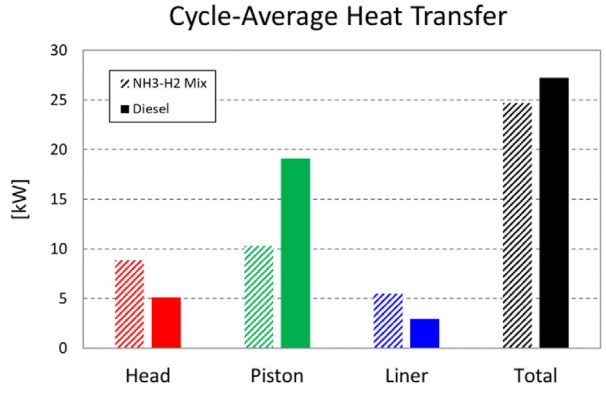

Fig. 22 – Cycle-Averaged heat transfer on the main boundaries facing the chamber.

4.5. *NO_x: a deepening by 1D and 3D results*

Results proposed in the previous paragraph point out a strong increase of the nitrogen oxides moving from Diesel to NH_3–H_2 80mol%-20mol% mixture, which is one of the most detrimental aspects relative to the use of ammonia-hydrogen mixtures. One of the reasons in the increase of the NO concentration with NH_3–H_2 mixtures is the use of a stoichiometric mixture. The latter is preferred both to rich mixtures to reduce the fuel consumption and to lean ones to avoid an extreme reduction of the LFS, already penalized by the use of ammonia. Nonetheless, an important information for engine designers is the value of Φ (if it exists) needed to eliminate (or at least reduce of orders of magnitude) the nitrogen oxides only acting on the mixture quality, while keeping the original engine performance. In order to obtain such information, 1D chemical kinetics and 3D in-cylinder simulations are exploited. In freely propagating flames, NO concentration depends on the distance from the flame brush position (as discussed in Appendix B), because the time available for the reactions changes. For this reason, in order to estimate a sensitivity to this parameter, different distances from the flame brush are considered in the following for the evaluation of the NO mass fractions. Making a parallel with the in-cylinder, it is the same as considering different time (or CA) intervals inside the combustion chamber.

In Fig. 23a) to 23d) NO mass fractions for the thermodynamic state 6 of Fig. 2, Shrestha mechanism and different mixtures are reported as a function of Φ, at different distances from the flame brush. As for the upper limit of Φ, NO values are not reported for an equivalence ratio greater than 1.2 as there is no interest in rich mixtures in order to keep the consumption as low as possible. As for the lean values of the equivalence ratio, the calculated NO mass fractions are limited by convergence criteria (i.e. it is not possible to obtain a stable solution for lower Φ values). Despite in Ref. [145] it is suggested that limits of convergence of laminar flame speed calculations well correspond to flammability limits, this criterion seems to be strongly influenced by numerics. In this regard, it is important to point out that the definition of the flammability limits is not straightforward at the conditions considered in the present study (values reported in Table 1 just refer to standard conditions). As reported in literature [146–151], pressure and temperature strongly influence lower and upper flammability limits. Moreover, as for the hydrogen, the impact of thermodynamic conditions is not clearly defined from the available studies [152,153]. Despite it is not possible

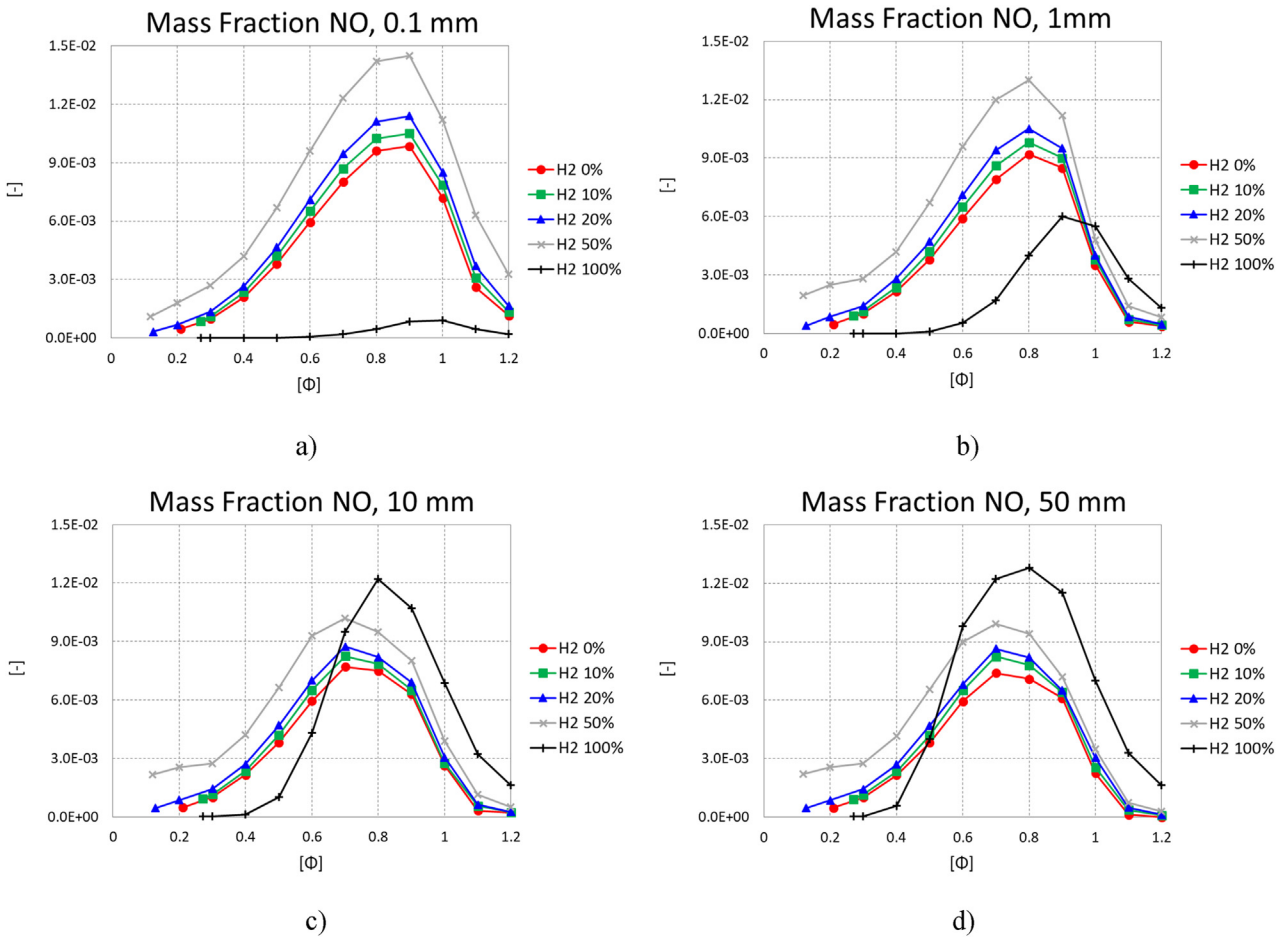

Fig. 23 – NO mass fraction for different mixtures and distances from the flame brush position: a) 0.1 *mm*, b) 1 *mm*, c) 10 *mm* and d) 50 *mm*. The analyzed condition is represented by the state 6 of Fig. 2. For brevity of the legend, the mixture H_2 0% corresponds to the NH_3–H_2 100mol%-0mol%, H_2 10% to the NH_3–H_2 90mol%-10mol% and similarly for the others.

to firmly state that extremal NO values on the lean side are at the flammability limit, it is still reasonable to affirm that they are close to it. This is important since, as visible in Fig. 23a) to 23d), even close to the lower flammability limit, it is not possible to eliminate NO or, at least, drastically reduce it to a negligible amount compared to the stoichiometric condition, with a NH_3–H_2 80mol%-20mol% mixture. In the same figure, NO mass fractions obtained with other mixtures are proposed as well and the final result is similar. Only pure hydrogen is able to work at lean conditions with a massive reduction of NO (at least of two orders of magnitude compared to the stoichiometric condition). However, as previously stated, pure hydrogen is not a preferable solution. The main reason of a non-negligible concentration of NO even at very low equivalence ratio values is the presence of NH_3. Compared to traditional fuels, for which NO_x formation is mainly due to a thermal mechanism, in case of NH_3 the formation is mainly related to the fuel composition as it contains nitrogen, whose atoms are released during combustion leading to NO_x formation together with oxygen. Unlike thermal NO_x which require very high temperature for the atmospheric N_2 reaction and prompt NO_x that need the presence of a hydrocarbon, fuel NO_x formation can take place at lower temperature (provided that the combustion occurs) as it is only related to the combustion reactions (in the flame front) that release the nitrogen contained in the fuel. This is confirmed by both Figs. 23 and 24. In fact, as visible in Fig. 23, considering for example an equivalence ratio of 0.8, for all the mixtures containing NH_3, the NO concentration decreases despite an increase of the distance from the flame brush. This is not typical of the thermal mechanism considering that, behind the flame front, temperature is very high and nearly constant as the flame is adiabatic. Similarly, Fig. 24a) shows the NO mass fraction for the sector simulation presented in the previous paragraphs with the NH_3–H_2 100mol%-0mol% mixture. The greatest concentration can be noticed in proximity of the flame front, while the highest temperature is in the core region as indicated by Fig. 24b).

A further confirmation comes from the pure hydrogen case. Since it does not contain nitrogen, H_2 is characterized by the lowest concentration of NO at very lean conditions, despite the highest adiabatic flame temperature (on equal Φ) compared to the other mixtures. The reason is that temperature is too low to lead to consistent NO formation. Then,

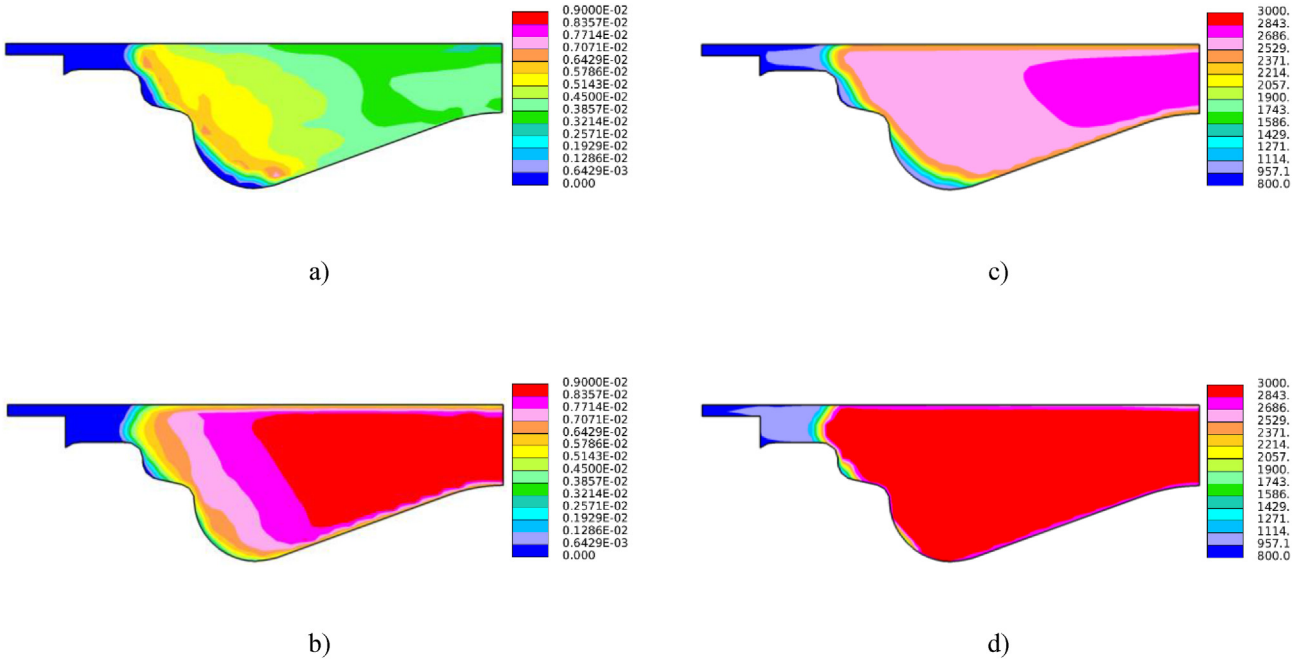

Fig. 24 – a) NO mass fraction and b) temperature (expressed in [K]) at 730° CA, obtained in the sector domain with the NH_3–H_2 100mol%-0mol% mixture and a spark timing of 705° CA; c) NO mass fraction and d) temperature (expressed in [K]) at 735° CA, obtained in the sector domain with the NH_3–H_2 0mol%-100mol% mixture and a spark timing of 722.5° CA.

moving to more stoichiometric conditions, the concentration of NO is higher increasing the hydrogen content (from pure NH_3 to pure H_2). This trend is confirmed by the experiments available in literature [53] and it is due to higher available temperatures (that enable the thermal mechanism) and to the H_2 adiabatic flame temperature which is the highest one. Another corroboration of the results interpretation comes from hydrogen behavior, which provides a NO mass concentration increasing with the distance from the brush (i.e. increasing the time available for the burnt gases to react). This behavior is coherent with the thermal mechanism of NO_x formation, which requires high temperature (available far from the brush as the flame is adiabatic) and time for the reactions to take place. Considering an in-cylinder combustion, this traduces in a higher concentration in the core of the domain (burnt region where temperature is maximum), rather than in the proximity of the flame front, as visible in Fig. 24c) and d), which show NO and temperature for the previously presented sector simulation with pure hydrogen.

A more feasible solution to limit the production of NO in case of ammonia-hydrogen blends would be the adoption of rich mixtures, as it can be inferred from Fig. 23a) to 23d). In fact, a strong reduction is already visible at $\Phi = 1.2$. This is also confirmed by literature [62]. However, besides the consumption issues cited at the beginning of the paragraph, the use of rich mixtures implies an increase of unburnt fuel at the exhaust (which should be avoided as well) thus it represents an impractical solution.

It is important to point out that the results are proposed in terms of mass fractions but roughly the same values and trends can be obtained considering mole fractions.

Further sensitivities (to thermodynamic state and chemical mechanism) are reported in Appendix E.

However, comparing NO mass fractions at different equivalence ratios on equal distance from the brush (or, alternatively, at a given equivalence ratio, comparing NO mass fractions for different mixtures on equal distance from the brush) may not be strictly rigorous. In fact, the LFS is strongly different and, on equal distance from the brush, the time available for the burnt gases to react modifies. This is far from the in-cylinder framework where, at some extent, the time available for the reactions is instead common (on equal spark time) for the different Φ or mixtures and it is limited by the EVO. Therefore, in order to confirm the 1D outcomes, results of a full-chamber in-cylinder simulation with NH_3–H_2 80%mol-20%mol mixture, characterized by an equivalence ratio of 0.4, are proposed in the following, to be compared with the previous ones characterized by stoichiometric mixture. Another important task of the 3D simulation is the check of the performance, which has to be kept despite the mixture quality variation. Even though a Φ value strongly lower than 0.4 should be investigated, this is not possible because of limits in the fitting polynomials of the laminar flame speeds. Fig. 25 shows a comparison between the pressure trace of the previously shown simulation (with $\Phi = 1$ and Shrestha chemical scheme) and the new curve (obtained with $\Phi = 0.4$). Diesel operation pressure trace is reported as well for comparison. Despite the differences in terms of pressure, performance is comparable between the two cases, as indicated by the Gross IMEP values reported in Fig. 15. Moreover, the maximum pressure remains slightly lower compared to the original Diesel engine, despite the huge increase of intake

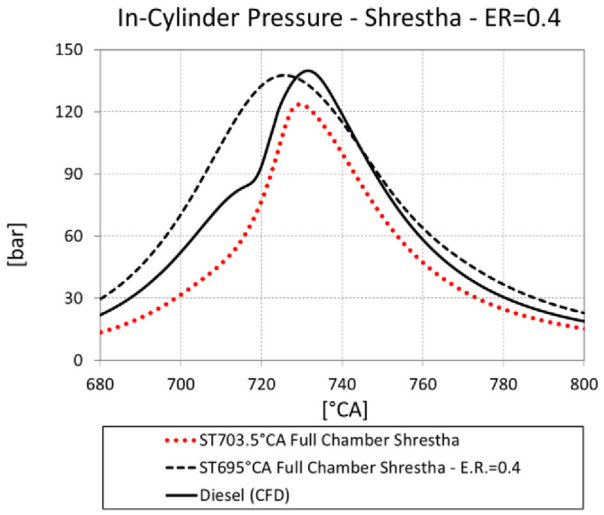

Fig. 25 – In-cylinder pressure for the mixture NH_3–H_2 80mol%-20mol% and the Shrestha mechanism. Results of both $\Phi = 1$ and $\Phi = 0.4$ cases are shown and, for comparison, Diesel one is reported as well.

pressure and trapped mass. Fig. 26a) shows the resulting NO concentration in terms of ppm, which confirms the decrease compared to the stoichiometric case, as anticipated by 1D outcomes of Figs. 23 and 37 (the latter placed in Appendix E). Interestingly, Fig. 26b) reports NO in terms of $g/\ kWh$ for the same case and, unlike ppm values, just a minimal reduction is noticed with $\Phi = 0.4$. The reason is that, although NO concentration is lower compared to the stoichiometric condition, the mass in the cylinder is strongly greater. In fact, in order to keep the same performance and considering that the latter depends on the fuel quantity, working at very lean conditions requires a greater amount of air + fuel mass. Therefore, despite the mass fraction of NO is lower, the total mass may not change remarkably or be even higher because of the increased amount of mass. In the light of this observations it is possible to state that:

- the 3D investigation confirms the 1D outcomes (which is not obvious as previously pointed out), thus for any ammonia-hydrogen blend there is no lean mixture able to drastically reduce NO concentration (even if further 3D investigations would be desirable at $\Phi < 0.4$);
- regardless the 1D outcomes, 3D simulations remain still necessary to check the performance and determine the mass of NO as working with 1D results, i.e. with concentrations alone, is misleading.

Fig. 27 shows a comparison in terms of temperature. Despite a strong reduction of the latter compared to the $\Phi = 1$ case, NO concentration is not characterized by a remarkable reduction, since the leading mechanism is not the thermal one. The result is even more noteworthy if the comparison is carried out against the Diesel operation curve. In fact, recovering NO concentration of the Diesel case from Fig. 5a), it results that NO production is strongly higher at $\Phi = 0.4$ despite a lower temperature.

Before the conclusions, it is useful to point out that working with very lean mixtures is not only potentially needless to reduce NO_x but, in order to obtain the required mass inside the cylinder (which is, as indicated in Table 3, at $\Phi = 0.4$, strongly greater than Diesel operation), a strong increase of the intake pressure is required. In the proposed case, boost pressure is equal to 3.8 $bar(a)$, thus much higher than Diesel operation. This may lead not only to an oversizing of the turbocharger compared to the original one, but also to a decrease of the engine efficiency. In this regard, the impact of the port fuel injection is minimal on the required boost pressure. In other words, moving to a direct injection would reduce the required boost pressure of nearly 0.2 bar (thanks to the presence of air alone at the intake) which is not sufficient to recover the original value of the Diesel operation. In addition, very lean mixtures cause an increase of in-cylinder pressure. In fact, in Fig. 25, the pressure trace referring to the Diesel case is

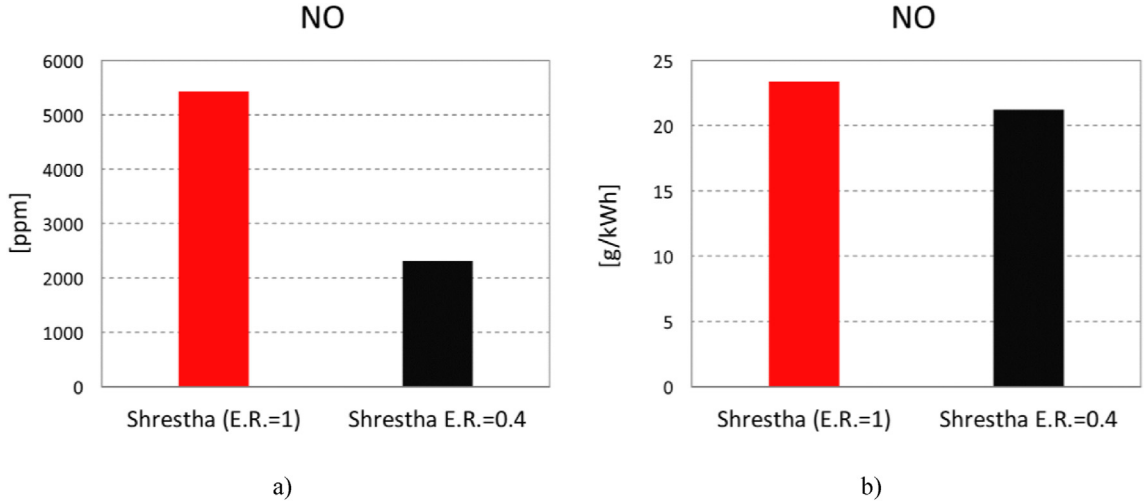

Fig. 26 – NO for the mixture NH_3–H_2 80mol%-20mol% and different equivalence ratios, 1 and 0.4; a) shows values in *ppm* while b) in *g/kWh*.

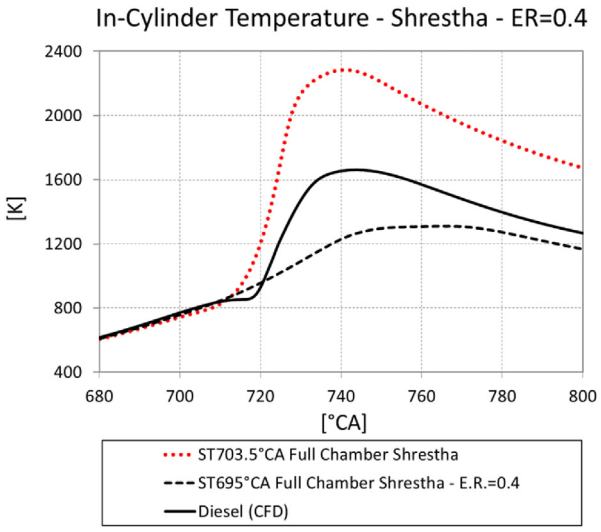

Fig. 27 – In-cylinder temperature for the mixture NH_3–H_2 80mol%-20mol% and the Shrestha mechanism. Results of both $\Phi = 1$ and $\Phi = 0.4$ cases are shown and, for comparison, Diesel one is reported as well.

reported as well, showing a comparable maximum pressure with respect to the ammonia-hydrogen case at $\Phi =$ 0.4. A leaner mixture would lead to an increase of maximum in-cylinder pressure (and thus of mechanical stress) compared to the original Diesel case.

Other points that remain open are the flammability limit and the combustion stability. Even if 3D outcomes at $\Phi <$ 0.4 confirmed a potential reduction of NO, the capability of the engine to work at very lean conditions should be checked. In fact, the very lean equivalence ratio values investigated via 1D simulations may be beyond the flammability limits of the mixtures or lead to very high COV. This can be assessed only via experiments.

5. Conclusions and future developments

The increasing concern against greenhouse gases, especially CO_2, is pushing towards the adoption of carbon free e-fuels, such as hydrogen and ammonia, to power internal combustion engines. Compared to pure hydrogen and pure ammonia, mixtures of the two can help to compensate their respective deficiencies. The present paper aims at providing an overall numerical framework to simulate combustion of pure NH_3, pure H_2 and NH_3–H_2 mixtures in internal combustion engines in order to predict performance, emissions, knock onset and heat transfer. The proposed numerical framework relies on 0D, 1D and 3D tools and it is applied to convert an existing marine Diesel engine. Besides a comprehensive framework to simulate combustion of NH_3–H_2 mixtures, the present paper provides, thanks to the proposed Diesel engine test case, practical hints for designers aiming at exploiting NH_3 and H_2 to convert existing powertrains. In the light of the poor combustion-related-properties of the ammonia (scarcely improved in case of small hydrogen additions), a stoichiometric condition is firstly accounted for. Apart from pure hydrogen which is limited by knock onset, pure ammonia and the investigated mixtures of the two are able to recover the same engine performance of the original Diesel version. However, considering aspects such as COV, MIE and autonomy, the NH_3–H_2 80mol%-20mol% mixture is selected as the best compromise and its results in terms of emissions and heat transfer are deeply investigated. While the resulting heat transfer is comparable to the original Diesel engine, a strong increase of NO_x is noticed with the use of the selected NH_3–H_2 mixture. A more detailed investigation via a combination of 1D and 3D simulations reveals that, as long as NH_3 is adopted as fuel, because of its nitrogen content, NO_x mass (or mole) fraction cannot be significantly (i.e. of orders of magnitude) reduced, even at very lean air-fuel mixtures (such as $\Phi = 0.2$). Therefore, the investigated NH_3–H_2 mixtures can be a valid alternative to traditional fossil fuels only if the problems in terms of autonomy and NO_x are solved (for example, with advanced storage and after-treatment systems) and their production relies on renewable sources.

As for the proposed numerical framework, further developments are reserved to future activities. In particular:

- The 1D framework can be improved with predictive models (for knock and emissions, besides the already available ones for turbulence and combustion) and then exploited, once validated/tuned against 3D outcomes, to investigate the whole engine map.
- An improved knock model can be adopted in 3D simulations to estimate knock statistics despite the RANS approach.
- LFS fitting polynomials for NH_3–H_2 mixtures able to account for very high pressure and temperatures, extremely lean equivalence ratios (<0.4) and EGR can be developed, so that extremely lean operations can be simulated via 3D-CFD to investigate NO_x formation.
- The ignition model can be refined, for example introducing the modeling of the electric circuit.
- Other chemical mechanisms can be investigated.
- The effect of the instabilities in the laminar flame speed correlations can be included.
- Validation against experiments is desirable.
- Development and validation of a unique combustion model (namely ECFM-3Z) able to simulate both traditional fuels and ammonia-hydrogen mixtures.

The framework can be applied, in the future, to investigate the same engine with pure hydrogen at very lean conditions ($\Phi < 0.3$), in order to check the possibility to keep the original Diesel engine performance (without knock occurrence) and estimate NO_x emissions. In fact, experiments confirm that, at very lean conditions, most of the hydrogen-related-drawbacks such as MIE and NO_x formation can be strongly reduced [154–156] and the use of a single fuel simplifies the hardware. In the light of this, apart from the storage that remains challenging, pure hydrogen would appear more (or not less) appealing than NH_3–H_2 mixtures. Conversely, the latter suffer, as shown in this paper, very high NO_x formation (even at very lean conditions) and the autonomy is double compared

to pure hydrogen but still widely lower (nearly a quarter) compared to Diesel fuel.

Declaration of competing interest

The authors declare that they have no known competing financial interests or personal relationships that could have appeared to influence the work reported in this paper.

Acknowledgment

The authors gratefully acknowledge the University of Modena and Reggio Emilia for supporting the activity by the "Fondo di Ateneo per la Ricerca 2022 per il finanziamento di piani di sviluppo dipartimentale nell'ambito della ricerca" (FARD 2022).

Appendix A. Supplementary data

Supplementary data to this article can be found online at https://doi.org/10.1016/j.ijhydene.2023.09.158.

REFERENCES

[1] European Commission. European Green Deal: commission proposes transformation of EU economy and society to meet climate ambitions. 2021.
[2] Santos G. Road transport and CO2 emissions: what are the challenges? Transp Policy (Oxf) 2017;59:71–4. https://doi.org/10.1016/j.tranpol.2017.06.007.
[3] Johnson T. Review of CO2 emissions and technologies in the road transportation sector. SAE Int J Engines Aug. 2010;3:1079–98. https://doi.org/10.4271/2010-01-1276.
[4] Pagliuso JD. 9 - biofuels for spark-ignition engines. In: Zhao H, editor. Advanced direct injection combustion engine technologies and development. Woodhead Publishing; 2010. p. 229–59. https://doi.org/10.1533/9781845697327.229.
[5] Khan A, et al. Investigation of biofuel as a potential renewable energy source. Atmosphere Oct. 2021;12:1289. https://doi.org/10.3390/atmos12101289.
[6] Janssen A, Muether M, Kolbeck A, Lamping M, Pischinger S. The impact of different biofuel components in diesel blends on engine efficiency and emission performance. In: SAE technical paper. SAE; 2010. https://doi.org/10.4271/2010-01-2119.
[7] Tripathi S, Villalta D, Monsalve-Serrano J, Antonio G. Electric vehicles vs e-fuelled ICE vehicles: comparison of potentials for life cycle CO2 emission reduction. Ma: SAE Technical Paper; r. 2022. https://doi.org/10.4271/2022-01-0745.
[8] Rothbart M. E-fuel production via renewables and the impact on the in-use CO 2 performance. In: SAE technical paper. SAE; Sep. 2020. https://doi.org/10.4271/2020-01-2139.
[9] Ababneh H, Hameed BH. Electrofuels as emerging new green alternative fuel: a review of recent literature. Energy Convers Manag 2022;254:115213. https://doi.org/10.1016/j.enconman.2022.115213.
[10] Pochet M, Truedsson I, Foucher F, Jeanmart H, Contino F. Ammonia-hydrogen blends in homogeneous-charge compression-ignition engine. SAE Technical Paper; Sep. 2017. https://doi.org/10.4271/2017-24-0087. 2017-24–0087.
[11] Verkamp FJ, Hardin MC, Williams JR. Ammonia combustion properties and performance in gas-turbine burners. Symp (International) Comb 1967;11(1):985–92. https://doi.org/10.1016/S0082-0784(67)80225-X.
[12] Shrestha KP, Seidel L, Zeuch T, Mauss F. Detailed kinetic mechanism for the oxidation of ammonia including the formation and reduction of nitrogen oxides. Energy Fuels Oct. 2018;32(10):10202–17. https://doi.org/10.1021/acs.energyfuels.8b01056.
[13] Takizawa K, Igarashi N, Takagi S, Tokuhashi K, Kondo S. Quenching distance measurement of highly to mildly flammable compounds. Fire Saf J 2015;71:58–68. https://doi.org/10.1016/j.firesaf.2014.11.013.
[14] Sileghem L, et al. Laminar burning velocity of gasoline and the gasoline surrogate components iso-octane, n-heptane and toluene. Fuel 2013;112:355–65. https://doi.org/10.1016/j.fuel.2013.05.049.
[15] Knop V, Benkenida A, Jay S, Colin O. Modelling of combustion and nitrogen oxide formation in hydrogen-fuelled internal combustion engines within a 3D CFD code. Int J Hydrogen Energy 2008;33(19):5083–97. https://doi.org/10.1016/j.ijhydene.2008.06.027.
[16] White CM, Steeper RR, Lutz AE. The hydrogen-fueled internal combustion engine: a technical review. Int J Hydrogen Energy 2006;31(10):1292–305. https://doi.org/10.1016/j.ijhydene.2005.12.001.
[17] Aleiferis PG, Rosati MF. Controlled autoignition of hydrogen in a direct-injection optical engine. Combust Flame 2012;159(7):2500–15. https://doi.org/10.1016/j.combustflame.2012.02.021.
[18] Teoh YH, et al. A review on production and implementation of hydrogen as a green fuel in internal combustion engines. Fuel 2023;333:126525. https://doi.org/10.1016/j.fuel.2022.126525.
[19] Mørch CS, Bjerre A, Gøttrup MP, Sorenson SC, Schramm J. Ammonia/hydrogen mixtures in an SI-engine: engine performance and analysis of a proposed fuel system. Fuel 2011;90(2):854–64. https://doi.org/10.1016/j.fuel.2010.09.042.
[20] Lhuillier C, Brequigny P, Contino F, Mounaïm-Rousselle C. Performance and emissions of an ammonia-fueled SI engine with hydrogen enrichment. In: SAE technical paper. SAE; Sep. 2019. https://doi.org/10.4271/2019-24-0137.
[21] Frigo S, Gentili R. Analysis of the behaviour of a 4-stroke Si engine fuelled with ammonia and hydrogen. Int J Hydrogen Energy 2013;38(3):1607–15. https://doi.org/10.1016/j.ijhydene.2012.10.114.
[22] Xin G, Ji C, Wang S, Meng H, Chang K, Yang J. Effect of different volume fractions of ammonia on the combustion and emission characteristics of the hydrogen-fueled engine. Int J Hydrogen Energy 2022;47(36):16297–308. https://doi.org/10.1016/j.ijhydene.2022.03.103.
[23] Inal OB, Zincir B, Deniz C. Investigation on the decarbonization of shipping: an approach to hydrogen and ammonia. Int J Hydrogen Energy 2022;47(45):19888–900. https://doi.org/10.1016/j.ijhydene.2022.01.189.
[24] Xin G, Ji C, Wang S, Meng H, Chang K, Yang J. Effect of ammonia addition on combustion and emission characteristics of hydrogen-fueled engine under lean-burn condition. Int J Hydrogen Energy 2022;47(16):9762–74. https://doi.org/10.1016/j.ijhydene.2022.01.027.
[25] Ji C, et al. Effect of ammonia addition on combustion and emissions performance of a hydrogen engine at part load and stoichiometric conditions. Int J Hydrogen Energy

2021;46(80):40143–53. https://doi.org/10.1016/j.ijhydene.2021.09.208.
[26] Wang B, Yang C, Wang H, Hu D, Wang Y. Effect of Diesel-Ignited Ammonia/Hydrogen mixture fuel combustion on engine combustion and emission performance. Fuel 2023;331:125865. https://doi.org/10.1016/j.fuel.2022.125865.
[27] Dinesh MH, Pandey JK, Kumar GN. Study of performance, combustion, and NOx emission behavior of an SI engine fuelled with ammonia/hydrogen blends at various compression ratio. Int J Hydrogen Energy 2022;47(60):25391–403. https://doi.org/10.1016/j.ijhydene.2022.05.287.
[28] Xu X, Liu E, Zhu N, Liu F, Qian F. Review of the current status of ammonia-blended hydrogen fuel engine development. Energies Jan. 2022;15:1023. https://doi.org/10.3390/en15031023.
[29] Fenn JB. Lean flammability limit and Minimum spark ignition energy. Commercial fluids and pure hydrocarbons. Ind Eng Chem Dec. 1951;43(12):2865–9. https://doi.org/10.1021/ie50504a057.
[30] Kurien C, Mittal M. Review on the production and utilization of green ammonia as an alternate fuel in dual-fuel compression ignition engines. Energy Convers Manag 2022;251:114990. https://doi.org/10.1016/j.enconman.2021.114990.
[31] Cardoso JS, Silva V, Rocha RC, Hall MJ, Costa M, Eusébio D. Ammonia as an energy vector: current and future prospects for low-carbon fuel applications in internal combustion engines. J Clean Prod 2021;296:126562. https://doi.org/10.1016/j.jclepro.2021.126562.
[32] Dimitriou P, Javaid R. A review of ammonia as a compression ignition engine fuel. Int J Hydrogen Energy 2020;45(11):7098–118. https://doi.org/10.1016/j.ijhydene.2019.12.209.
[33] Tornatore C, Marchitto L, Sabia P, De Joannon M. Ammonia as green fuel in internal combustion engines: state-of-the-art and future perspectives. Front Mech Eng 2022;8 [Online]. Available: https://www.frontiersin.org/articles/10.3389/fmech.2022.944201.
[34] Erdemir D, Dincer I. A perspective on the use of ammonia as a clean fuel: challenges and solutions. Int J Energy Res Mar. 2021;45(4):4827–34. https://doi.org/10.1002/er.6232.
[35] Zhou L, Zhong L, Liu Z, Wei H. Toward highly-efficient combustion of ammonia–hydrogen engine: prechamber turbulent jet ignition. Fuel 2023;352:129009. https://doi.org/10.1016/j.fuel.2023.129009.
[36] Manigandan S, Ryu JI, Praveen Kumar TR, Elgendi M. Hydrogen and ammonia as a primary fuel – a critical review of production technologies, diesel engine applications, and challenges. Fuel 2023;352:129100. https://doi.org/10.1016/j.fuel.2023.129100.
[37] Kurien C, Mittal M. Utilization of green ammonia as a hydrogen energy carrier for decarbonization in spark ignition engines. Int J Hydrogen Energy 2023;48(74):28803–23. https://doi.org/10.1016/j.ijhydene.2023.04.073.
[38] Zhang X, Moosakutty SP, Rajan RP, Younes M, Sarathy SM. Combustion chemistry of ammonia/hydrogen mixtures: jet-stirred reactor measurements and comprehensive kinetic modeling. Combust Flame 2021;234:111653. https://doi.org/10.1016/j.combustflame.2021.111653.
[39] He X, Shu B, Nascimento D, Moshammer K, Costa M, Fernandes RX. Auto-ignition kinetics of ammonia and ammonia/hydrogen mixtures at intermediate temperatures and high pressures. Combust Flame 2019;206:189–200. https://doi.org/10.1016/j.combustflame.2019.04.050.
[40] Chen X, Liu Q, Zhao W, Li R, Zhang Q, Mou Z. Experimental and chemical kinetic study on the flame propagation characteristics of ammonia/hydrogen/air mixtures. Fuel 2023;334:126509. https://doi.org/10.1016/j.fuel.2022.126509.
[41] Wang N, et al. Laminar burning characteristics of ammonia/hydrogen/air mixtures with laser ignition. Int J Hydrogen Energy 2021;46(62):31879–93. https://doi.org/10.1016/j.ijhydene.2021.07.063.
[42] Xin G, et al. Experimental study of the effect of variable valve timing on hydrogen-enriched ammonia engine. Fuel 2023;344:128131. https://doi.org/10.1016/j.fuel.2023.128131.
[43] Xin G, et al. Experimental study on Miller cycle hydrogen-enriched ammonia engine by rich-burn strategy. Fuel 2023;350:128899. https://doi.org/10.1016/j.fuel.2023.128899.
[44] Hong C, Ji C, Wang S, Xin G, Qiang Y, Yang J. Evaluation of hydrogen injection and oxygen enrichment strategies in an ammonia-hydrogen dual-fuel engine under high compression ratio. Fuel 2023;354:129244. https://doi.org/10.1016/j.fuel.2023.129244.
[45] Dinesh MH, Kumar GN. Experimental investigation of variable compression ratio and ignition timing effects on performance, combustion, and Nox emission of an ammonia/hydrogen-fuelled Si engine. Int J Hydrogen Energy 2023. https://doi.org/10.1016/j.ijhydene.2023.05.219.
[46] Hong C, et al. An experimental study of a strategy to improve the combustion process of a hydrogen-blended ammonia engine under lean and WOT conditions. Int J Hydrogen Energy 2023. https://doi.org/10.1016/j.ijhydene.2023.05.122.
[47] Li J, Zhang R, Pan J, Wei H, Shu G, Chen L. Ammonia and hydrogen blending effects on combustion stabilities in optical SI engines. Energy Convers Manag 2023;280:116827. https://doi.org/10.1016/j.enconman.2023.116827.
[48] Westlye FR, Ivarsson A, Schramm J. Experimental investigation of nitrogen based emissions from an ammonia fueled SI-engine. Fuel 2013;111:239–47. https://doi.org/10.1016/j.fuel.2013.03.055.
[49] Frigo S, Gentili R, Doveri N. Ammonia plus hydrogen as fuel in a S.I. Engine: experimental results, vol. 4. *SAE Technical Paper*; Oct. 2012. https://doi.org/10.4271/2012-32-0019.
[50] Pyrc M, Gruca M, Tutak W, Jamrozik A. Assessment of the co-combustion process of ammonia with hydrogen in a research VCR piston engine. Int J Hydrogen Energy 2023;48(7):2821–34. https://doi.org/10.1016/j.ijhydene.2022.10.152.
[51] Ji C, et al. Effect of ammonia addition on combustion and emissions performance of a hydrogen engine at part load and stoichiometric conditions. Int J Hydrogen Energy 2021;46(80):40143–53. https://doi.org/10.1016/j.ijhydene.2021.09.208.
[52] Xin G, Ji C, Wang S, Meng H, Chang K, Yang J. Effect of ammonia addition on combustion and emission characteristics of hydrogen-fueled engine under lean-burn condition. Int J Hydrogen Energy 2022;47(16):9762–74. https://doi.org/10.1016/j.ijhydene.2022.01.027.
[53] Lhuillier C, Brequigny P, Contino F, Mounaïm-Rousselle C. Experimental study on ammonia/hydrogen/air combustion in spark ignition engine conditions. Fuel 2020;269:117448. https://doi.org/10.1016/j.fuel.2020.117448.
[54] Pochet M, Jeanmart H, Contino F. A 22:1 compression ratio ammonia-hydrogen HCCI engine: combustion, load, and emission performances. Front Mech Eng 2020;6. https://doi.org/10.3389/fmech.2020.00043.
[55] Comotti M, Frigo S. Hydrogen generation system for ammonia–hydrogen fuelled internal combustion engines. Int J Hydrogen Energy 2015;40(33):10673–86. https://doi.org/10.1016/j.ijhydene.2015.06.080.
[56] Frigo S, Gentili R, Angelis F. Further insight into the possibility to fuel a SI engine with ammonia plus hydrogen,

vol. 2014. SAE Technical Paper; Nov. 2014. https://doi.org/10.4271/2014-32-0082.
[57] Pozzana G, et al. A hybrid vehicle powered by hydrogen and ammonia, vol. 4. SAE Technical Paper; Oct. 2012. https://doi.org/10.4271/2012-32-0085.
[58] Yang W, Ranga Dinesh KKJ, Luo KH, Thevenin D. Direct numerical simulation of turbulent premixed ammonia and ammonia-hydrogen combustion under engine-relevant conditions. Int J Hydrogen Energy 2022;47(20):11083–100. https://doi.org/10.1016/j.ijhydene.2022.01.142.
[59] Otomo J, Koshi M, Mitsumori T, Iwasaki H, Yamada K. Chemical kinetic modeling of ammonia oxidation with improved reaction mechanism for ammonia/air and ammonia/hydrogen/air combustion. Int J Hydrogen Energy 2018;43(5):3004–14. https://doi.org/10.1016/j.ijhydene.2017.12.066.
[60] Wang Y, Zhou X, Liu L. Study on the mechanism of the ignition process of ammonia/hydrogen mixture under high-pressure direct-injection engine conditions. Int J Hydrogen Energy 2021;46(78):38871–86. https://doi.org/10.1016/j.ijhydene.2021.09.122.
[61] Goldmann A, Dinkelacker F. Approximation of laminar flame characteristics on premixed ammonia/hydrogen/nitrogen/air mixtures at elevated temperatures and pressures. Fuel 2018;224:366–78. https://doi.org/10.1016/j.fuel.2018.03.030.
[62] Zhang F, Chen G, Wu D, Li T, Zhang Z, Wang N. Characteristics of ammonia/hydrogen premixed combustion in a novel linear engine generator. Proc West Mark Ed Assoc Conf Sep. 2020;58:2. https://doi.org/10.3390/WEF-06925.
[63] Wang D, Ji C, Wang S, Yang J, Wang Z. Numerical study of the premixed ammonia-hydrogen combustion under engine-relevant conditions. Int J Hydrogen Energy 2021;46(2):2667–83. https://doi.org/10.1016/j.ijhydene.2020.10.045.
[64] Liang W, Law CK. Enhancing ammonia combustion using reactivity stratification with hydrogen addition. Proc Combust Inst 2023;39(4):4419–26. https://doi.org/10.1016/j.proci.2022.10.025.
[65] Gaucherand J, Laera D, Schulze-Netzer C, Poinsot T. Intrinsic instabilities of hydrogen and hydrogen/ammonia premixed flames: influence of equivalence ratio, fuel composition and pressure. Combust Flame 2023;256:112986. https://doi.org/10.1016/j.combustflame.2023.112986.
[66] Bayramoğlu K, Bahlekeh A, Masera K. Numerical investigation of the hydrogen, ammonia and methane fuel blends on the combustion emissions and performance. Int J Hydrogen Energy 2023. https://doi.org/10.1016/j.ijhydene.2023.06.079.
[67] Yang W, Ranga Dinesh KKJ, Luo KH, Thévenin D. Direct numerical simulations of auto-igniting mixing layers in ammonia and ammonia-hydrogen combustion under engine-relevant conditions. Int J Hydrogen Energy 2022;47(89):38055–74. https://doi.org/10.1016/j.ijhydene.2022.08.290.
[68] Frankl S, Gleis S, Karmann S, Prager M, Wachtmeister G. Investigation of ammonia and hydrogen as CO2-free fuels for heavy duty engines using a high pressure dual fuel combustion process. Int J Engine Res Sep. 2020;22. https://doi.org/10.1177/1468087420967873.
[69] Wang Y, Zhou X, Liu L. Feasibility study of hydrogen jet flame ignition of ammonia fuel in marine low speed engine. Int J Hydrogen Energy 2023;48(1):327–36. https://doi.org/10.1016/j.ijhydene.2022.09.198.
[70] Wang B, Yang C, Wang H, Hu D, Duan B, Wang Y. Study on injection strategy of ammonia/hydrogen dual fuel engine under different compression ratios. Fuel 2023;334:126666. https://doi.org/10.1016/j.fuel.2022.126666.
[71] Zhang H, et al. Numerical study on combustion and emission characteristics of a spark-ignition ammonia engine added with hydrogen-rich gas from exhaust-fuel reforming. Fuel 2023;332:125939. https://doi.org/10.1016/j.fuel.2022.125939.
[72] Wang Y, Zhou X, Liu L. Theoretical investigation of the combustion performance of ammonia/hydrogen mixtures on a marine diesel engine. Int J Hydrogen Energy 2021;46(27):14805–12. https://doi.org/10.1016/j.ijhydene.2021.01.233.
[73] Wang B, Wang H, Duan B, Yang C, Hu D, Wang Y. Effect of ammonia/hydrogen mixture ratio on engine combustion and emission performance at different inlet temperatures. Energy 2023;272:127110. https://doi.org/10.1016/j.energy.2023.127110.
[74] Wang H, Wang B, Yang C, Hu D, Duan B, Wang Y. Study on dual injection strategy of diesel ignition ammonia/hydrogen mixture fuel engine. Fuel 2023;348:128526. https://doi.org/10.1016/j.fuel.2023.128526.
[75] Novella R, Pastor J, Gomez-Soriano J, Sánchez-Bayona J. Numerical study on the use of ammonia/hydrogen fuel blends for automotive spark-ignition engines. Fuel 2023;351:128945. https://doi.org/10.1016/j.fuel.2023.128945.
[76] Ge H, Bakir AH, Zhao P. Knock mitigation and power enhancement of hydrogen spark-ignition engine through ammonia blending. Machines 2023. https://doi.org/10.3390/machines11060651.
[77] Mattarelli E, et al. Combustion optimization of a marine DI diesel engine. In: SAE Technical Papers, 6; Sep. 2013. https://doi.org/10.4271/2013-24-0020.
[78] Teodosio L, Berni F, Lanotte A, Malfi E. 1D/3D simulation procedure to investigate the potential of a lean burn hydrogen fuelled engine. J Phys Conf Ser 2022;2385(1):12085. https://doi.org/10.1088/1742-6596/2385/1/012085.
[79] Costa J, Martins J, Arantes T, Gonçalves M, Durão L, Brito F. Experimental assessment of the performance and emissions of a spark-ignition engine using waste-derived biofuels as additives. Energies Aug. 2021;14:5209. https://doi.org/10.3390/en14165209.
[80] SIEMENS PLM. DARS v2020.1 manual - book 2. 2020.
[81] Klippenstein SJ, Harding LB, Glarborg P, Miller JA. The role of NNH in NO formation and control. Combust Flame 2011;158(4):774–89. https://doi.org/10.1016/j.combustflame.2010.12.013.
[82] Song Y, et al. The sensitizing effects of NO2 and NO on methane low temperature oxidation in a jet stirred reactor. Proc Combust Inst 2019;37(1):667–75. https://doi.org/10.1016/j.proci.2018.06.115.
[83] Stagni A, et al. An experimental, theoretical and kinetic-modeling study of the gas-phase oxidation of ammonia. React Chem Eng 2020;5(4):696–711. https://doi.org/10.1039/C9RE00429G.
[84] Stagni A, et al. Low- and intermediate-temperature ammonia/hydrogen oxidation in a flow reactor: experiments and a wide-range kinetic modeling. Chem Eng J 2023;471:144577. https://doi.org/10.1016/j.cej.2023.144577.
[85] Cicci F, d'Adamo A, Barbato A, Breda S. Comparison of library-based and detailed chemistry models for knock prediction in spark-ignition engines. In: AIP conference proceedings; Dec. 2019. p. 20046. https://doi.org/10.1063/1.5138779.
[86] Göttgens J, Mauss F, Peters N. Analytic approximations of burning velocities and flame thicknesses of lean hydrogen, methane, ethylene, ethane, acetylene, and propane flames. Symp (International) Comb 1992;24(1):129–35. https://doi.org/10.1016/S0082-0784(06)80020-2.

[87] SIEMENS PLM. DARS v2020.1 manual - book 4. 2020.
[88] Ranzi E, Cavallotti C, Cuoci A, Frassoldati A, Pelucchi M, Faravelli T. New reaction classes in the kinetic modeling of low temperature oxidation of n-alkanes. Combust Flame 2015;162(5):1679–91. https://doi.org/10.1016/j.combustflame.2014.11.030.
[89] Bagheri G, Ranzi E, Pelucchi M, Parente A, Frassoldati A, Faravelli T. Comprehensive kinetic study of combustion technologies for low environmental impact: MILD and OXY-fuel combustion of methane. Combust Flame 2020;212:142–55. https://doi.org/10.1016/j.combustflame.2019.10.014.
[90] Ranzi E, Frassoldati A, Stagni A, Pelucchi M, Cuoci A, Faravelli T. Reduced kinetic schemes of complex reaction systems: fossil and biomass-derived transportation fuels. Int J Chem Kinet Sep. 2014;46(9):512–42. https://doi.org/10.1002/kin.20867.
[91] Vervisch PE, Colin O, Michel J-B, Darabiha N. NO Relaxation Approach (NORA) to predict thermal NO in combustion chambers. Combust Flame 2011;158(8):1480–90. https://doi.org/10.1016/j.combustflame.2010.12.014.
[92] Gamma Technologies. GT-suite manuals - version 7.5. 2016.
[93] Heywood JB. Internal combustion engine fundamentals. 1988. New York,.
[94] Bozza F, De Bellis V, Berni F, d'Adamo A, Maresca L. Refinement of a 0D turbulence model to predict tumble and turbulent intensity in SI engines. Part I: 3D analyses. In: SAE technical paper; Apr. 2018. https://doi.org/10.4271/2018-01-0850.
[95] Bozza F, Teodosio L, De Bellis V, Fontanesi S, Iorio A. Refinement of a 0D turbulence model to predict tumble and turbulent intensity in SI engines. Part II: model concept, validation and discussion. In: SAE technical paper; Apr. 2018. https://doi.org/10.4271/2018-01-0856.
[96] Teodosio L, Berni F. Optimization via genetic algorithm of a variable-valve-actuation spark-ignition engine based on the integration between 1D/3D simulation codes and optimizer. Int J Engine Res May 2022:14680874221099874. https://doi.org/10.1177/14680874221099874.
[97] Bozza F, De Bellis V, Berni F, D'Adamo A, Maresca L. Refinement of a 0D turbulence model to predict tumble and turbulent intensity in SI engines. Part I: 3D analyses. In: SAE technical paper; 2018. https://doi.org/10.4271/2018-01-0850.
[98] Bozza F, Gimelli A, Merola S, Vaglieco BM. Validation of a fractal combustion model through flame imaging, vol. 114. SAE Technical Paper; Apr. 2005. https://doi.org/10.4271/2005-01-1120.
[99] SIEMENS PLM. STARCD v4.34 manual - methodology. 2020.
[100] Yakhot V, Orszag SA. Renormalization group analysis of turbulence. I. Basic theory. J Sci Comput 1986;1(1):3–51. https://doi.org/10.1007/BF01061452.
[101] Berni F, Fontanesi S. A 3D-CFD methodology to investigate boundary layers and assess the applicability of wall functions in actual industrial problems: a focus on in-cylinder simulations. Appl Therm Eng 2020;174:115320. https://doi.org/10.1016/j.applthermaleng.2020.115320.
[102] Berni F, Cicalese G, Sparacino S, Cantore G. On the existence of universal wall functions in in-cylinder simulations using a low-Reynolds RANS turbulence model. AIP Conf Proc Dec. 2019;2191(1):20019. https://doi.org/10.1063/1.5138752.
[103] Berni F, Cicalese G, Borghi M, Fontanesi S. Towards grid-independent 3D-CFD wall-function-based heat transfer models for complex industrial flows with focus on in-cylinder simulations. Appl Therm Eng 2021;190:116838. https://doi.org/10.1016/j.applthermaleng.2021.116838.
[104] Berni F, Cicalese G, Fontanesi S. A modified thermal wall function for the estimation of gas-to-wall heat fluxes in CFD in-cylinder simulations of high performance spark-ignition engines. Appl Therm Eng 2017;115. https://doi.org/10.1016/j.applthermaleng.2017.01.055.
[105] Cicalese G, Berni F, Fontanesi S, D'Adamo A, Andreoli E. A comprehensive CFD-CHT methodology for the characterization of a Diesel engine: from the heat transfer prediction to the thermal field evaluation. SAE Technical Paper; 2017. https://doi.org/10.4271/2017-01-2196. 2017-Octob.
[106] Angelberger C, Poinsot T, Delhay B. Improving near-wall combustion and wall heat transfer modeling in SI engine computations. In: SAE technical paper; 1997. https://doi.org/10.4271/972881.
[107] Cicalese G, Berni F, Fontanesi S. Integrated in-cylinder/CHT methodology for the simulation of the engine thermal field: an application to high performance turbocharged DISI engines. SAE Int J Engines 2016;9(1). https://doi.org/10.4271/2016-01-0578.
[108] Senda J, Kanda T, Al-Roub M, V Farrell P, Fukami T, Fujimoto H. Modeling spray impingement considering fuel film formation on the wall. SAE Trans 1997;106:98–112. https://doi.org/10.4271/970047.
[109] Habchi C. A comprehensive model for liquid film boiling in internal combustion engines. Oil Gas Sci Tech– Rev. IFP Mar. 2010;65(2):331–43. https://doi.org/10.2516/ogst/2009062.
[110] Colin O, Benkenida A. The 3-zones extended coherent flame model (Ecfm3z) for computing premixed/diffusion combustion. Oil Gas Sci Tech- Rev. IFP 2004;59(6):593–609. https://doi.org/10.2516/ogst:2004043.
[111] D'Adamo A, Breda S, Berni F, Fontanesi S. Understanding the origin of cycle-to-cycle variation using large-eddy simulation: similarities and differences between a homogeneous low-revving speed research engine and a production DI turbocharged engine. SAE Int J Engines 2018;12(1):45–56. https://doi.org/10.4271/03-12-01-0007.
[112] Severi E, D'Adamo A, Berni F, Breda S, Lugli M, Mattarelli E. Numerical investigation on the effects of bore reduction in a high performance turbocharged GDI engine. 3D investigation of knock tendency. Energy Procedia; 2015. p. 846–55. https://doi.org/10.1016/j.egypro.2015.12.094.
[113] Shekhawat Y, et al. An experimental and simulation study of early flame development in a homogeneous-charge spark-ignition engine. Oil Gas Sci Technol 2017;72(5). https://doi.org/10.2516/ogst/2017028.
[114] Subramanian G, Pires da Cruz A, Colin O, Vervisch L. Modeling engine turbulent auto-ignition using tabulated detailed chemistry. In: SAE technical paper; Apr. 2007. https://doi.org/10.4271/2007-01-0150.
[115] Pei Y, Mehl M, Liu W, Lu T, Pitz W, Som S. A multi-component blend as a diesel fuel surrogate for compression ignition engine applications. J Eng Gas Turbines Power Nov. 2015;137. https://doi.org/10.1115/1.4030416.
[116] Jenkins RA, Holmberg RW, Wike JS, Moneyhun JH, Brazell RS. Chemical characterization and toxicologic evaluation of airborne mixtures. Chem Phys Char Dies Fuel Smoke 1984 [Online]. Available: https://www.osti.gov/biblio/6840016.
[117] Aubagnac-Karkar D, Michel J-B, Colin O, Vervisch-Kljakic PE, Darabiha N. Sectional soot model coupled to tabulated chemistry for Diesel RANS simulations. Combust Flame 2015;162(8):3081–99. https://doi.org/10.1016/j.combustflame.2015.03.005.
[118] Marchal C, Moréac G, Vovelle C, Mounaïm-Rousselle C, Mauss F. Soot modelling in automotive engines. In: Proceedings of the European combustion meeting; Dec. 2009 [Online]. Available: https://www.researchgate.net/

profile/Fabian-Mauss/publication/268367829_Soot_modelling_in_automotive_engines/links/54b91cd30cf269d8cbf731bf/Soot-modelling-in-automotive-engines.pdf.
[119] Berni F, et al. Modeling of gaseous emissions and soot in 3D-CFD in-cylinder simulations of spark-ignition engines: a methodology to correlate numerical results and experimental data. Int J Engine Res Jul. 2022:14680874221112564. https://doi.org/10.1177/14680874221112564.
[120] Stefano Sfriso, Fabio Berni, Stefano Fontanesi, Alessandro d'Adamo, Marco Antonelli, Stefano Frigo. A 3D-CFD numerical approach for combustion simulations of spark ignition engines fuelled with hydrogen: a preliminary analysis. In: SAE technical paper; 2023. https://doi.org/10.4271/2023-01-0207.
[121] Ewald J, Peters N. On unsteady premixed turbulent burning velocity prediction in internal combustion engines. Proc Combust Inst 2007;31(2):3051–8. https://doi.org/10.1016/j.proci.2006.07.119.
[122] Peters N. Turbulent combustion. Cambridge: Cambridge University Press; 2000. https://doi.org/10.1017/CBO9780511612701.
[123] Yang S, Reitz RD, Iyer CO, Yi J. Improvements to combustion models for modeling spark-ignition engines using the G-equation and detailed chemical kinetics. SAE Int J Fuels Lubr 2009;1(1):1009–25. https://doi.org/10.4271/2008-01-1634.
[124] Liang L, Reitz R. Spark ignition engine combustion modeling using a level set method with detailed chemistry. In: SAE technical paper; May 2006. https://doi.org/10.4271/2006-01-0243.
[125] Pessina V, Berni F, Fontanesi S, Stagni A, Mehl M. Laminar flame speed correlations of ammonia/hydrogen mixtures at high pressure and temperature for combustion modeling applications. Int J Hydrogen Energy Jun. 2022;47. https://doi.org/10.1016/j.ijhydene.2022.06.007.
[126] Hernandez Ignacio, Turquand d'Auzay Charles, Richard Penning, Shapiro Evgeniy, Hughes John. Thermo-diffusive flame speed adjustment and its application to hydrogen engines. SAE Technical Paper; 2023. https://doi.org/10.4271/2023-01-0197.
[127] Hirasawa T, Sung CJ, Joshi A, Yang Z, Wang H, Law CK. Determination of laminar flame speeds using digital particle image velocimetry: binary Fuel blends of ethylene, n-Butane, and toluene. Proc Combust Inst 2002;29(2):1427–34. https://doi.org/10.1016/S1540-7489(02)80175-4.
[128] Elbaz AM, Wang S, Guiberti TF, Roberts WL. Review on the recent advances on ammonia combustion from the fundamentals to the applications. Fuel Commun 2022;10:100053. https://doi.org/10.1016/j.jfueco.2022.100053.
[129] Bruneaux G. Asymptotic analysis, direct numerical simulation and modeling of premixed turbulent flame-wall interaction; Etude asymptotique, simulation numerique directe et modelisation de l'interaction flamme turbulente premelangee-paroi. Ph.D. Thesis. Institut Francais du Petrole (IFP), 92 - Rueil-Malmaison (France); 1996.
[130] Lee M, Hall M, Ezekoye O, Matthews R. Voltage, and energy deposition characteristics of spark ignition systems. A: SAE Technical Paper; pr. 2005. https://doi.org/10.4271/2005-01-0231.
[131] Huang S, Li T, Ma P, Xie S, Zhang Z, Chen R. Quantitative evaluation of the breakdown process of spark discharge for spark-ignition engines. J Phys D Appl Phys 2020;53(4):45501. https://doi.org/10.1088/1361-6463/ab56da.
[132] Stevens CR. Energy storage and the criteria for proper ignition in the internal combustion engine. IEEE Trans Ind Electron Control Instrum 1965;IECI-12(1):8–13. https://doi.org/10.1109/TIECI.1965.229542.
[133] Tambasco C, Hall M, Matthews R. Spark discharge characteristics for varying spark plug geometries and gas compositions. In: SAE technical paper; Mar. 2022. https://doi.org/10.4271/2022-01-0437.
[134] Arora Ravindra, Mosch Wolfgang. High voltage and electrical insulation engineering. 2nd ed. 2022. 2nd Edition.
[135] Liao L, et al. A novel gas sensor based on field ionization from ZnO nanowires: moderate working voltage and high stability. Nanotechnology Apr. 2008;19:175501. https://doi.org/10.1088/0957-4484/19/17/175501.
[136] Meek JM, Craggs JD. Electrical breakdown of gases. A Wiley-Interscience publication. Wiley; 1978 [Online]. Available: https://books.google.it/books?id=1Xp5AAAAIAAJ.
[137] Modi A, Koratkar N, Lass E, Wei B, Ajayan PM. Miniaturized gas ionization sensors using carbon nanotubes. Nature 2003;424(6945):171–4. https://doi.org/10.1038/nature01777.
[138] Herweg R, Maly RR. A fundamental model for flame kernel formation in S. I. Engines. SAE Trans 1992;101:1947–76. https://doi.org/10.4271/922243.
[139] Breda S, et al. CFD analysis of combustion and knock in an optically accessible GDI engine. SAE Int J Engines Apr. 2016;9:649–64. https://doi.org/10.4271/2016-01-0601.
[140] Livengood JC, Wu PC. Correlation of autoignition phenomena in internal combustion engines and rapid compression machines. Symp (International) Comb 1955;5(1):347–56. https://doi.org/10.1016/S0082-0784(55)80047-1.
[141] Colin O, Truffin K. A spark ignition model for large eddy simulation based on an FSD transport equation (ISSIM-LES). Proc Combust Inst 2011;33(2):3097–104. https://doi.org/10.1016/j.proci.2010.07.023.
[142] Stępień Z. A comprehensive overview of hydrogen-fueled internal combustion engines: achievements and future challenges. Energies Oct. 2021;14:6504. https://doi.org/10.3390/en14206504.
[143] Verhelst S, Wallner T. Hydrogen-fueled internal combustion engines. Prog Energy Combust Sci 2009;35(6):490–527. https://doi.org/10.1016/j.pecs.2009.08.001.
[144] del Pecchia M, Pessina V, Berni F, d'Adamo A, Fontanesi S. Gasoline-ethanol blend formulation to mimic laminar flame speed and auto-ignition quality in automotive engines. Fuel 2020;264. https://doi.org/10.1016/j.fuel.2019.116741.
[145] Mascarenhas VJ, Weber CN, Westmoreland PR. Estimating flammability limits through predicting non-adiabatic laminar flame properties. Proc Combust Inst 2021;38(3):4673–81. https://doi.org/10.1016/j.proci.2020.06.026.
[146] Harris GFP, Macdermott PE. Flammability and explosibility of ammonia. 1964 [Online]. Available: https://www.icheme.org/media/10569/vi-paper-04.pdf.
[147] Zlochower IA. Experimental flammability limits and associated theoretical flame temperatures as a tool for predicting the temperature dependence of these limits. J Loss Prev Process Ind 2012;25(3):555–60. https://doi.org/10.1016/j.jlp.2011.12.012.
[148] Kondo S, Takizawa K, Takahashi A, Tokuhashi K. On the temperature dependence of flammability limits of gases. J Hazard Mater 2011;187(1):585–90. https://doi.org/10.1016/j.jhazmat.2011.01.037.
[149] Pio G, Salzano E. Flammability limits of methane (LNG) and hydrogen (LH2) at extreme conditions. Chem Eng Trans Nov. 2019;77:601–6. https://doi.org/10.3303/CET1977101.
[150] Mendiburu AZ, de Carvalho JA, Coronado CR, Roberts JJ. Flammability limits temperature dependence of pure

compounds in air at atmospheric pressure. Energy 2017;118:414–24. https://doi.org/10.1016/j.energy.2016.12.036.
[151] Ciccarelli G, Jackson D, Verreault J. Flammability limits of NH3–H2–N2–air mixtures at elevated initial temperatures. Combust Flame 2006;144(1):53–63. https://doi.org/10.1016/j.combustflame.2005.06.010.
[152] Shapiro ZM, Moffette TR. Hydrogen flammability data and application to Pwr loss-of-coolant accident. 1957. https://doi.org/10.2172/4327402. United States.
[153] Liu X, Zhang Q. Influence of initial pressure and temperature on flammability limits of hydrogen–air. Int J Hydrogen Energy 2014;39(12):6774–82. https://doi.org/10.1016/j.ijhydene.2014.02.001.
[154] Bao L, Sun B, Luo Q. Experimental investigation of the achieving methods and the working characteristics of a near-zero NOx emission turbocharged direct-injection hydrogen engine. Fuel 2022;319:123746. https://doi.org/10.1016/j.fuel.2022.123746.
[155] Bao L, Sun B, Luo Q. Optimal control strategy of the turbocharged direct-injection hydrogen engine to achieve near-zero emissions with large power and high brake thermal efficiency. Fuel 2022;325:124913. https://doi.org/10.1016/j.fuel.2022.124913.
[156] Ono R, Nifuku M, Fujiwara S, Horiguchi S, Oda T. Minimum ignition energy of hydrogen–air mixture: effects of humidity and spark duration. J Electrost 2007;65(2):87–93. https://doi.org/10.1016/j.elstat.2006.07.004.